JTSES
Journal of Thermal and Sustainable Energy Systems
https://jtses.com/index.php/home/index

Functionally Graded Medium-Entropy Alloy Coatings for Hydrogen-Assisted Cryogenic Fatigue Resistance of Stainless Steel

Sujitha Angamuthu [1], S. Krishnakumar [2], P. Balashanmuga Vadivu [3], S. Nanthakumar [4]

[1] Department of Electronics and Communication Engineering, Paavai Engineering College, Namakkal – 637018, Tamil Nadu, India — Email: ersujitha.a@gmail.com

[2] Department of Mechanical Engineering, Gnanamani College of Technology, Pachal, Namakkal – 637018, Tamil Nadu, India — Email: krishk92@gmail.com

[3] Department of Electronics and Communication Engineering, Mahendra Engineering College (Autonomous), Namakkal – 637503, Tamil Nadu, India — Email: shanmugavadivup@mahendra.info

[4] Department of Mechanical Engineering, Paavai College of Engineering, Namakkal – 637018, Tamil Nadu, India — Email: nanthasnk126@gmail.com

Corresponding Author*: Sujitha Angamuthu — Email: ersujitha.a@gmail.com

ABSTRACT

Hydrogen-facing stainless-steel components are subjected to hydrogen ingress, cryogenic deformation, cyclic loading, and thermal gradients that challenge uniform coatings. A route to distribute interfacial compliance, hydrogen management, and surface durability is offered by compositionally graded CoCrFeNiMo architectures. The coupled effects of CoCrFeNiMo grading on phase stability, hydrogen transport, and cryogenic fatigue damage in 316L stainless steel have not been resolved. The objective of this work is to establish a composition–structure–hydrogen–fatigue framework for a directed-energy-deposited graded CoCrFeNiMo/316L system. Thermodynamic descriptors, CALPHAD-informed phase analysis, DED thermal modelling, diffusion–trapping formulations, and fatigue-mechanics relationships were integrated with literature-constrained validation. Six CoCrFeNiMo $_{x}$ compositions were evaluated while unsupported measurements were excluded. Configurational entropy rose from 11.526 to 13.381 J mol $^{-1}$ K $^{-1}$, atomic-size mismatch rose from 0.302% to 3.671%, and VEC shifted from 8.250 to 7.800. A nominal linear DED energy input of 228.0 J mm $^{-1}$ was obtained from the reference process condition. An FCC-rich inner region, an intermediate transition, and a Mo-rich surface region are supported as a mechanistically consistent graded architecture. Compositionally resolved design for hydrogen-assisted cryogenic fatigue service is enabled by the framework. Future research is directed toward experimental validation of hydrogen trapping, phase connectivity, residual stress, and fatigue crack evolution.

KEYWORDS: Directed energy deposition, CoCrFeNiMo gradient coating, Hydrogen diffusion–trapping, Cryogenic fatigue, 316L stainless steel

INTRODUCTION

Hydrogen-service components used in storage, transfer, and cryogenic propulsion were subjected simultaneously to hydrogen ingress, low temperature, cyclic stress, and steep thermal gradients, so coating design required more than conventional hardness or corrosion optimisation. Temperature-dependent hydrogen embrittlement in VCoNi demonstrated that cryogenic resistance depended strongly on deformation mode and hydrogen redistribution rather than on low temperature alone [1]. For CoCrFeNiMo-based alloys, laser melting deposition already provided a direct processing route toward low-temperature service: CoCrFeNiMo $_{0.2}$ produced at 1400 W reached 928 MPa tensile strength and approximately 60% ductility at 77 K, while corrosion resistance exceeded that of conventional stainless-steel comparators under the reported conditions [2]. Laser-directed energy deposition of CoCrFeNi likewise preserved a single-phase FCC matrix while generating columnar grains and high dislocation density; cooling from 293 to 77 K raised the reported yield and ultimate tensile strengths to 565 and 965 MPa, respectively, with deformation twinning becoming dominant at 77 K [3]. Hydrogen transport nevertheless remained microstructure-sensitive: nanoindentation-based diffusion analysis of DED CoCrNi and 316L showed that apparently similar FCC alloys could display different hydrogen diffusivities and hydrogen-induced hardness responses because solution energetics and vacancy interactions differed [4]. ()

Recent hydrogen studies further showed why compositionally complex alloys could not simply be classified as intrinsically hydrogen resistant. Controlled gaseous charging revealed that equiatomic VCoNi absorbed substantially more hydrogen than 316L and CrCoNi and could undergo severe intergranular cleavage when hydrogen penetrated throughout the specimen, demonstrating strong dependence on charging methodology and hydrogen distribution [5]. Conversely, an additively manufactured CrCoNi/TiC composite maintained comparatively strong hydrogen-embrittlement resistance at both room and cryogenic temperatures, with the response linked to hydrogen trapping and temperature-dependent HELP/HEDE contributions [6]. LPBF CoCrNi exhibited characteristic hydrogen-induced intergranular cracking, while EBSD and TEM revealed contributions from subgrain boundaries, local grain refinement, and hydrogen-enhanced deformation twinning [7]. Coherent $L1_2$ precipitation combined with grain-boundary boron segregation restricted diffusible hydrogen and intergranular cracking in a CoCrNi-based alloy [8]. Carbon–boron–chromium co-segregation similarly suppressed gaseous-hydrogen embrittlement by strengthening boundaries and limiting hydrogen accumulation, confirming that trap character and interface cohesion mattered as much as total hydrogen uptake [9]. These hydrogen-response studies complemented the coating literature summarised in Table 1, where laser-processing route, phase selection, compositional grading, and Mo-driven intermetallic formation emerged as the principal design variables.

Table 1:**studies defining processing–composition–microstructure relationships in laser-deposited high- and medium-entropy alloy systems.**

Objective/Aim	Methodology/Approach	Materials/Parameters Studied	Key Findings/Results	Relevance to Current Study
Couple wear resistance with interfacial reliability	Laser cladding; SEM; nanoindentation; XPS; wear testing	H13–CoCrFeNi–CoCrFeNiMo; 500 °C wear	△ 678.6 HV hardness; ▽ wear volume ~83%	Closest graded CoCrFeNi/CoCrFeNiMo coating precedent [10]
Characterise additively manufactured eutectic CoCrFeNiMo	DED; microscopy; phase analysis; hardness; tribology	Equiatomic CoCrFeNiMo; build-height thermal history	△ 658.44 HV; FCC–σ–μ eutectic established	Direct DED processing evidence for target chemistry [11]
Evaluate high-speed clad CoCrFeNiMo coating	High-speed cladding; XRD; microscopy; nanoindentation; electrochemistry	CoCrFeNiMo; phase morphology; corrosion response	△ fine 2–5 μm grains; dual phases	Supports rapid-cladding phase and corrosion control[12]
Resolve laser-power effects on tribological performance	Laser cladding; XRD; microscopy; high-temperature wear	CoCrFeNiMo; laser power; temperatures to 800 °C	△ oxide-glaze protection; ▽ high-temperature wear	Links processing, σ phase, hardness, surface durability [13]
Quantify Mo-dependent coating behaviour	Extreme-speed cladding; microscopy; hardness; thermal tribology	$CoCrFeNiMo_x$; x = 0–1; 25–800 °C	△ hardness 190–600 HV; ▽ Mo_1 wear rate	Constrains Mo-gradient surface composition[14]

Explain solidification across laser-clad interface	Laser cladding; simulation; microscopy; phase analysis	CoCrFeNiMo $_{0.2}$Nb $_{0.2}$; H13; scanning speed	△ eutectic evolution; (Mo)NbC boundary precipitation	Demonstrates thermal-gradient-controlled phase transitions [15]
Balance strength and toughness through grading	Laser cladding; EBSD; elevated-temperature compression	FeCoCrNiMnAl $_{0.5}$–FeCoCrNiMnAl gradient	△ strength–toughness balance; ▽ cracking tendency	Establishes mechanical rationale for graded HEA layers [16]
Compare high-speed and conventional cladding	Two cladding routes; EBSD; hardness; electrochemistry	CoCrFeMnNi; process-speed effects; Q235 substrate	△ grain refinement; ▽ dilution and crack sensitivity	Supports rapid-processing control of coating integrity[17]
Assess Nb-modified coatings on stainless steel	Laser cladding; XRD; microscopy; hardness; corrosion	CoCrFeNiNb $_{x}$; 316 stainless steel; x = 0–0.3	△ hardness and lattice parameter with Nb	Confirms entropy-alloy cladding compatibility with 316 steel [18]
Determine annealing-driven phase and property evolution	Laser cladding; annealing; phase analysis; tribology; corrosion	CoCrFeMoNi; 700–900 °C annealing	△ σ/μ redistribution; ▽ friction versus H13	Highlights post-solidification intermetallic sensitivity [19]

Hydrogen tolerance also depended on whether trapping structures assisted deformation or created mechanically vulnerable interfaces. A dual heterogeneous CoCrNi-based structure combined high-dislocation-density regions with coherent L1 $_{2}$ particles, and both populations acted as hydrogen traps while crack deflection occurred at heterogeneous interfaces (Liu et al., 2025). () In LPBF CoCrFeNi, solidification-cell boundaries trapped hydrogen in the as-built state, whereas annealing at 1100 °C dissolved the cells and promoted more homogeneous slip, illustrating that additive-manufacturing defects could be either kinetically beneficial or mechanically detrimental depending on their stability [20]. Boron segregation in CoCrFeNi lowered the reported hydrogen-embrittlement index from approximately 82% to 32%, while atom-probe tomography, thermal desorption, Ag decoration, and nanoindentation connected the change to grain-boundary chemistry, hydrogen occupancy, and slip transfer [21]. Pre-straining of CoCrNi likewise generated dense twin boundaries that acted as hydrogen traps and diffusion barriers, redirecting hydrogen away from grain boundaries and suppressing intergranular fracture [22]. Collectively, these observations indicated that an effective graded coating required spatial control over phase stability, trap population, plastic compatibility, and interfacial cohesion rather than indiscriminate maximisation of Mo content or hardness.

Cyclic loading imposed a further constraint because hydrogen altered both crack initiation and propagation. In-situ hydrogen charging produced a stress-amplitude-dependent fatigue response in 316L: crack-initiation life was extended at higher amplitudes but shortened at lower amplitudes as hydrogen altered planar slip and cross-slip behaviour [23]. () Acoustic-emission monitoring of hydrogen-charged 316L linked AE energy-release rate with fatigue-crack propagation and showed that hydrogen promoted secondary cracking and more irregular crack paths [24]. Strain-controlled testing of pre-charged 316L associated shorter fatigue life with hydrogen-assisted dislocation accumulation and twinning across strain amplitudes of 0.3–0.9% [25]. An EBSD-based crystal-plasticity framework later coupled hydrogen diffusion, trapping, and fatigue indicators and predicted hydrogen-charged 316L crack-initiation life within a reported ±1.5 scatter band . At cryogenic temperature, carbon-doped

CoCrFeMnNi reached a reported fatigue strength of 620 MPa at 10^6cycles at 77 K versus 460 MPa at 293 K [26]. () LPBF CrCoNi similarly showed stronger high-cycle fatigue performance at 150 K, associated with earlier and denser deformation twinning . Crack-growth experiments on CrCoNi across 293, 198, and 77 K further established strong grain-size and temperature effects on near-threshold fatigue propagation [27].

Laser cladding and DED therefore dominated coating fabrication, while XRD, SEM/EDS, EBSD, nanoindentation, and tribological testing dominated structure–property assessment . Hydrogen studies increasingly combined controlled charging with TDS, microscopy, and local mechanical measurements to distinguish trapping from embrittling interfaces . Cryogenic investigations consistently highlighted deformation twinning as an important source of low-temperature damage tolerance in FCC concentrated alloys . Hydrogen-fatigue studies, however, showed that cyclic response depended strongly on charging mode, stress or strain amplitude, and the partitioning of total life between crack initiation and propagation . The resulting literature therefore favoured mechanism-resolved assessment over single-property ranking, particularly when hydrogen transport, microstructure, and cyclic deformation interacted.

The field had consequently progressed from uniform entropy-alloy coatings toward controlled phase architectures, local chemical segregation, engineered trapping structures, and microstructure-sensitive fatigue models. Yet most coating studies remained centred on hardness, corrosion, or tribology, whereas most hydrogen and cryogenic studies examined bulk or additively manufactured alloys rather than compositionally graded protective layers on 316L. The evidence therefore pointed toward service-environment-driven gradient design rather than composition optimisation for a single isolated property.

Existing studies did not resolve how a through-thickness CoCrFeNiMo compositional gradient simultaneously controlled dilution, residual-stress accommodation, FCC/σ/μ phase development, hydrogen diffusion and trapping, and cryogenic fatigue-crack initiation on 316L. The closest graded CoCrFeNi/CoCrFeNiMo architecture was validated primarily through interfacial and tribological performance rather than hydrogen-assisted cyclic loading (Yu et al., 2026). () Hydrogen diffusivity measurements remained sensitive to material state and measurement methodology (Lee et al., 2023). () Fatigue studies on 316L treated hydrogen gradients through experimental or computational frameworks without incorporating a graded entropy-alloy coating (Zhao et al., 2026). () AE-based crack assessment established hydrogen-sensitive fatigue signatures but did not resolve multiple failure modes within a graded metallic coating/substrate system (He et al., 2025). () Cryogenic MEA studies also remained composition- and process-specific, leaving limited validation of scalable DED gradients under combined hydrogen and cyclic thermal–mechanical exposure (Hwang et al., 2025). ()

The present study differentiated the material architecture by spatially programming CoCrFeNiMo chemistry across a DED coating on 316L so that substrate-side compliance, an intermediate hydrogen-management region, and a wear-resistant exterior were analysed within one continuous system. Processing variables were coupled with composition- and phase-sensitive thermodynamic descriptors, microstructural characterisation, hydrogen permeation and trapping measurements, and room-temperature and cryogenic mechanical testing. Hydrogen-assisted fatigue behaviour was connected directly to crack initiation, interfacial damage, and fracture-path evolution, while acoustic-emission features were interpreted against physically verified damage modes rather than treated solely as statistical classification outputs. This framework also provided matched homogeneous-coating and uncoated controls so that effects arising from compositional grading could be separated from those produced by chemistry or laser processing alone.

The objective of the present study is to determine how a compositionally graded CoCrFeNiMo coating produced by directed energy deposition on 316L stainless steel controls phase evolution, hydrogen transport and trapping, interfacial integrity, and hydrogen-assisted cryogenic fatigue damage while enabling acoustic-emission-based identification of the governing failure mechanisms.

2. Materials and Methods

2.1. Study design and materials architecture

An integrated computational–experimental methodology was established to evaluate a compositionally graded Co–Cr–Fe–Ni–Mo coating architecture for hydrogen-assisted cryogenic fatigue protection of AISI 316L stainless

steel. The material concept was based on progressive modification of Ni and Mo contents through the coating thickness so that substrate compatibility, hydrogen-management capability, cryogenic deformation tolerance, and surface durability could be considered within a single metallurgically bonded architecture. The coating concept, hydrogen-exposure routes, cryogenic mechanical assessment, microstructural characterization, thermal-desorption analysis, and acoustic-emission-based damage discrimination were derived from the defined study framework.

The methodology was divided into four coupled levels. First, the composition space was screened by thermodynamic and electronic descriptors. Second, equilibrium and non-equilibrium phase stability were evaluated within a CALPHAD framework. Third, directed-energy-deposition (DED) thermal history and hydrogen diffusion–trapping behaviour were represented computationally. Finally, the modelling framework was linked to hydrogen permeation, microstructural characterization, cryogenic fatigue, fracture, and acoustic-emission observables. The complete methodological sequence was summarized schematically in Figure 1.

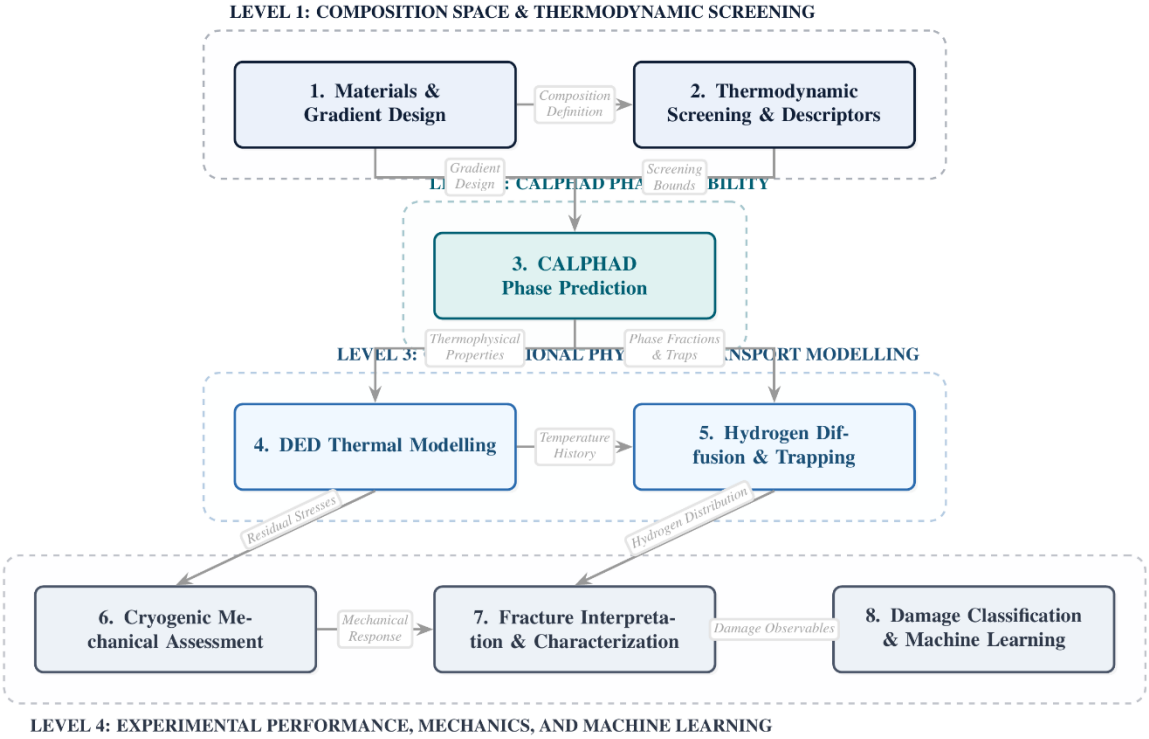

Figure 1: **Integrated methodology used for compositionally graded Co–Cr–Fe–Ni–Mo/316L assessment.**

The through-thickness architecture was represented by three chemically continuous functional regions rather than by an abrupt coating/substrate transition. A Ni-weighted substrate-side region was used to represent the comparatively ductile and chemically compatible interlayer, a compositionally intermediate region was used to represent the hydrogen-management zone, and progressively greater Mo weighting was imposed toward the external region to represent the strengthening and surface-durability contribution. The resulting architecture was illustrated in Figure 2. Absolute Ni and Mo contents were not assigned arbitrarily when specimen-specific powder-feed records were unavailable; instead, the gradient was represented continuously through local composition fields and was evaluated over a bounded composition space.

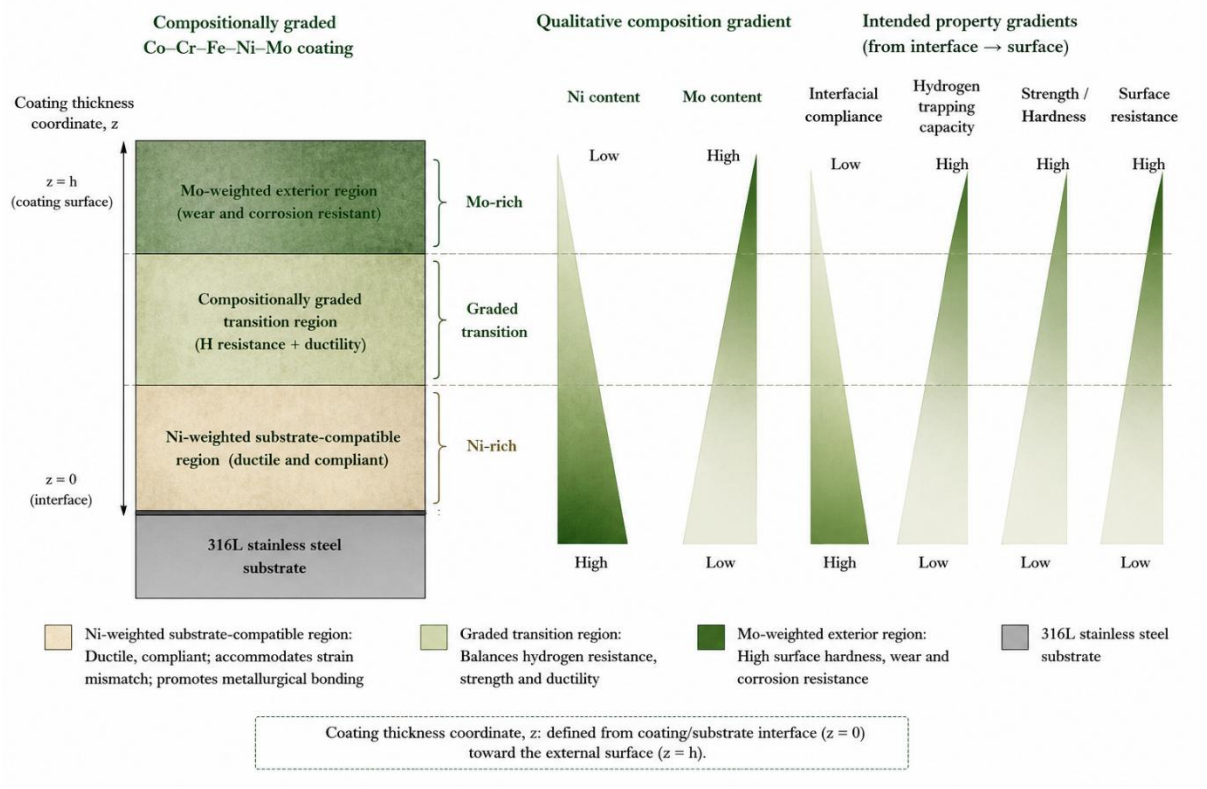

Figure 2:**Schematic representation of the compositionally graded Co–Cr–Fe–Ni–Mo coating on 316L stainless steel.**

The coating thickness coordinate, z, was defined from the coating/substrate interface toward the external surface. A Ni-weighted substrate-compatible region, a compositionally graded transition region, and a Mo-weighted exterior region were represented. The schematic was designed to display the corresponding qualitative gradients in Ni and Mo concentration together with the intended variations in interfacial compliance, hydrogen trapping, strength, and surface resistance.

2.2. Nominal alloy compositions and through-thickness gradient parameterization

The composition space was represented generally as $CoCrFeNi_yMo_x$, where xand ywere used as composition variables associated with the Mo and Ni fractions, respectively. For primary thermodynamic screening of the Mo contribution, six $CoCrFeNiMo_x$ anchor compositions were evaluated at $x = 0, 0.2, 0.4, 0.6, 0.8$, and 1.0. These states were used to span the transition from the equimolar CoCrFeNi base composition to the equimolar five-component CoCrFeNiMo composition. Ni redistribution was treated as an additional through-thickness composition variable rather than being replaced by an unsupported fixed numerical sequence.

For the $CoCrFeNiMo_x$ screening compositions, the total molar amount was expressed as $4 + x$, and the nominal atomic fractions were calculated as

$$c_{Co} = c_{Cr} = c_{Fe} = c_{Ni} = \frac{1}{4+x},\ c_{Mo} = \frac{x}{4+x}. \qquad (1)$$

Here, $c_i$was defined as the atomic fraction of constituent i, and the condition

$$\sum_{i=1}^{n} c_i = 1 \qquad (2)$$

was imposed for every evaluated composition.

Mass fractions were subsequently obtained from

$$w_i = \frac{c_i M_i}{\sum_{j=1}^{n} c_j M_j}, \qquad (3)$$

where $w_i$was defined as the mass fraction of element i, $M_i$was defined as its standard atomic mass, and nwas defined as the number of constituent elements. Standard atomic weights reported by the National Institute of Standards and Technology were used in the conversion [1]. ()

The resulting nominal atomic and calculated mass fractions were summarized in Table 2. These values were composition-derived quantities and were not treated as chemical analyses of deposited specimens.

Table 2:**Nominal atomic and calculated mass compositions of the CoCrFeNiMo $_x$ states used for thermodynamic screening.**

Alloy state	x	Co (at.%)	Cr (at.%)	Fe (at.%)	Ni (at.%)	Mo (at.%)	Co (wt.%)	Cr (wt.%)	Fe (wt.%)	Ni (wt.%)	Mo (wt.%)
Mo $_0$	0.0	25.00	25.00	25.00	25.00	0.00	26.14	23.06	24.77	26.03	0.00
Mo $_{0.2}$	0.2	23.81	23.81	23.81	23.81	4.76	24.09	21.25	22.83	23.99	7.84
Mo $_{0.4}$	0.4	22.73	22.73	22.73	22.73	9.09	22.34	19.71	21.17	22.25	14.55
Mo $_{0.6}$	0.6	21.74	21.74	21.74	21.74	13.04	20.82	18.37	19.73	20.74	20.34
Mo $_{0.8}$	0.8	20.83	20.83	20.83	20.83	16.67	19.50	17.20	18.48	19.42	25.40
Mo $_{1.0}$	1.0	20.00	20.00	20.00	20.00	20.00	18.34	16.18	17.37	18.26	29.85

For representation of the physical coating gradient, a normalized through-thickness coordinate was introduced as

$$\xi = \frac{z}{h}, \; 0 \le \xi \le 1, \qquad (4)$$

where zwas defined as the distance from the coating/substrate interface and hwas defined as the total coating thickness.

The local Mo and Ni composition fields were represented in their simplest continuous form by

$$c_{Mo}(\xi) = c_{Mo}^{in} + \left(c_{Mo}^{out} - c_{Mo}^{in}\right)\xi, \qquad (5)$$

and

$$c_{Ni}(\xi) = c_{Ni}^{in} + \left(c_{Ni}^{out} - c_{Ni}^{in}\right)\xi. \qquad (6)$$

Here, the superscripts “in” and “out” were used for the substrate-side and surface-side compositions, respectively. Piecewise-linear forms were permitted when discrete powder-feed transitions were represented. Local Co, Cr, and Fe fractions were subsequently normalized so that Eq. (2) remained satisfied at every through-thickness position.

When individual elemental powder-feed rates were available, local atomic fractions were calculated directly from the mass-feed rates as

$$c_i(z) = \frac{\dot{m}_i(z)/M_i}{\sum_j \dot{m}_j(z)/M_j}, \qquad (7)$$

where $\dot{m}_i(z)$was defined as the local mass-feed rate of element or feedstock i. This formulation allowed an experimentally implemented Ni/Mo feed schedule to be transferred directly into the thermodynamic and transport calculations without requiring an assumed concentration profile.

2.3. Thermodynamic, atomic-size, and electronic descriptors

Ideal configurational entropy was calculated for every composition because the entropy classification was required to be established from the actual local chemistry rather than from the nominal alloy name. The configurational entropy of mixing was calculated as

$$\Delta S_{mix} = -R \sum_{i=1}^{n} c_i \ln c_i , \qquad (8)$$

where $R = 8.314 J\ mol^{-1}\ K^{-1}$ was used as the universal gas constant.

The values calculated for the six primary $CoCrFeNiMo_x$ compositions were summarized in Table 3. A progressive increase in ΔS_{mix} was obtained as the composition approached the equimolar five-component state. Consequently, entropy classification was assigned composition by composition rather than by assuming that every point within the graded material belonged to one entropy category.

Valence-electron concentration was calculated from

$$VEC = \sum_{i=1}^{n} c_i (VEC)_i, \qquad (9)$$

where $(VEC)_i$ was defined as the elemental valence-electron contribution. Values of 9, 6, 8, 10, and 6 were assigned to Co, Cr, Fe, Ni, and Mo, respectively. VEC was used only as an electronic descriptor of FCC/BCC tendency and was not used as a standalone phase-identification criterion, in accordance with established HEA phase-screening approaches [2,3]. ()

Table 3:**Composition-derived configurational entropy and valence-electron concentration of the $CoCrFeNiMo_x$ screening states.**

Alloy state	**x**	**$\Delta S_{mix}/R$**	**ΔS_{mix}(J mol $^{-1}$ K $^{-1}$)**	**VEC**
Mo_0	0.0	1.386	11.526	8.250
$Mo_{0.2}$	0.2	1.512	12.568	8.143
$Mo_{0.4}$	0.4	1.565	13.011	8.045
$Mo_{0.6}$	0.6	1.593	13.242	7.957
$Mo_{0.8}$	0.8	1.606	13.351	7.875
$Mo_{1.0}$	1.0	1.609	13.381	7.800

Chemical interaction effects were evaluated from the mixing enthalpy,

$$\Delta H_{mix} = 4 \sum_{i=1}^{n-1} \sum_{j=i+1}^{n} \Delta H_{ij}^{mix} c_i c_j, \qquad (10)$$

where ΔH_{ij}^{mix} was defined as the binary liquid-state mixing enthalpy between elements iand j. A single internally consistent binary-interaction dataset was used throughout the calculations so that changes introduced by mixing incompatible parameter compilations were avoided.

Atomic-size mismatch was evaluated from

$$\bar{r} = \sum_{i=1}^{n} c_i r_i, \qquad (11)$$

followed by

$$\delta = 100\sqrt{\sum_{i=1}^{n} c_i\left(1-\frac{r_i}{\bar{r}}\right)^2}, \qquad (12)$$

where $r_i$was defined as the metallic radius of constituent iand $\bar{r}$was defined as the composition-weighted average radius.

The composition-weighted melting temperature was calculated as

$$T_m = \sum_{i=1}^{n} c_i\, T_{m,i}, \qquad (13)$$

and the entropy–enthalpy stability parameter was subsequently calculated from

$$\Omega = \frac{T_m \Delta S_{mix}}{|\Delta H_{mix}|}. \qquad (14)$$

The combined Ω–δ framework was used as a comparative solid-solution screening tool. The commonly reported region of $\Omega \geq 1.1$and $\delta \leq 6.6\%$was used as a reference boundary rather than as an absolute phase-selection rule [2]. ()

Electronegativity mismatch was calculated as

$$\bar{\chi} = \sum_{i=1}^{n} c_i\, \chi_i, \qquad (15)$$

and

$$\Delta\chi = \sqrt{\sum_{i=1}^{n} c_i\,(\chi_i - \bar{\chi})^2}, \qquad (16)$$

where $\chi_i$was defined as the Pauling electronegativity of constituent i. The descriptors obtained from Eqs. (8)–(16) were evaluated collectively so that configurational, chemical, geometric, and electronic contributions were considered simultaneously.

2.4. CALPHAD phase-equilibrium and non-equilibrium solidification analysis

Composition-dependent phase stability was evaluated within a CALPHAD framework. Thermodynamic calculations were defined using the Thermo-Calc high-entropy-alloy database TCHEA9, while mobility-dependent calculations were supported by MOBHEA4. These databases included Co, Cr, Fe, Ni, and Mo and were designed for multicomponent high-entropy and multi-principal-element alloy calculations [4]. ()

Equilibrium phase fractions were evaluated as functions of temperature for each nominal CoCrFeNiMo $_x$ state and for selected intermediate Ni/Mo gradient compositions. The fully liquid region, solidification interval, and low-temperature solid-state region were included so that liquidus temperature, solidus temperature, phase-appearance temperature, and phase-fraction evolution could be identified.

Non-equilibrium solidification was evaluated by Scheil-type calculations. Complete mixing was imposed in the liquid, whereas long-range solid-state diffusion was neglected during incremental solidification. Where mobility information was available, back-diffusion sensitivity was additionally considered. Particular attention was directed toward FCC solid solution and possible BCC, σ, μ, and other topologically close-packed phases because Mo enrichment had been associated with substantial changes in the phase constitution of CoCrFeNiMo-based materials.

The calculated equilibrium and Scheil phase fractions were exported as temperature-dependent datasets. Phase fractions were then interpolated as functions of both temperature and local composition so that thermodynamic predictions could be transferred to the DED thermal model and hydrogen-transport calculations. No phase was assigned solely from VEC, Ω, or δ; phase identification was instead based on the combined thermodynamic prediction.

2.5. Directed-energy-deposition reference condition and thermal modelling

A transient three-dimensional thermal formulation was used to represent the DED process. Because specimen-specific deposition records had not been provided as experimentally measured inputs, literature-derived processing values were used only as the reference condition for model construction. Gas-atomized equimolar CoCrFeNiMo powder with a reported particle-size range of approximately 75–150 μm had previously been deposited successfully onto 316L stainless steel by DED [5]. A laser power of 950 W, a scanning speed of 250 mm min $^{-1}$, a powder-feed rate of 9.5 g min $^{-1}$, and a nominal layer increment of 0.30 mm were adopted from that processing window as reference thermal-model inputs rather than as newly measured deposition parameters. ()

The reference model inputs were summarized in Table 4 so that literature-derived quantities remained distinguishable from composition-derived and specimen-specific quantities.

Table 4:**Literature-referenced inputs used for construction of the DED thermal model.**

Parameter	Reference value	Role in analysis	Data classification
Substrate	AISI 316L stainless steel	Thermal and mechanical substrate domain	Literature-defined
Feedstock	Equimolar CoCrFeNiMo powder	Reference deposited material	Literature-defined
Powder size	approximately 75–150 μm	Feedstock description	Literature-derived
Laser power	950 W	Heat-source input	Literature-derived
Scan speed	250 mm min $^{-1}$	Moving-source velocity	Literature-derived
Powder-feed rate	9.5 g min $^{-1}$	Reference deposition condition	Literature-derived
Nominal layer increment	0.30 mm	Geometric activation increment	Literature-derived
Ni/Mo gradient	$c_{Ni}(z)$, $c_{Mo}(z)$	Composition field	Model-defined
Thermal properties	$k(T, c)$, $C_p(T, c)$, $\rho(T, c)$	Heat-transfer solution	Literature/CALPHAD/model-derived

The transient thermal field was calculated from conservation of energy,

$$\rho(T, \mathbf{c})C_p(T, \mathbf{c})\frac{\partial T}{\partial t} = \nabla \cdot [k(T, \mathbf{c})\nabla T] + Q(\mathbf{x}, t), \qquad (17)$$

where ρwas defined as density, $C_p$was defined as specific heat capacity, kwas defined as thermal conductivity, Twas defined as temperature, twas defined as time, **c**was defined as the local composition vector, and Qwas defined as the moving volumetric heat input.

A Goldak-type double-ellipsoidal source was used to represent asymmetric heat deposition [6]. The volumetric source for the front and rear ellipsoids was expressed as

$$q_{f/r} = \frac{6\sqrt{3}\, f_{f/r}\eta P}{abc_{f/r}\pi\sqrt{\pi}} \exp\left[-3\left(\frac{x'^2}{a^2} + \frac{y'^2}{b^2} + \frac{z'^2}{c_{f/r}^2}\right)\right], \qquad (18)$$

subject to

$$f_f + f_r = 2. \qquad (19)$$

Here, Pwas defined as laser power, ηwas defined as effective absorptivity, a, b, c_f, and $c_r$were defined as geometric heat-source parameters, $f_f$and $f_r$were defined as the front and rear energy-distribution coefficients, and x', y', and z'were defined in the moving heat-source coordinate system. The double-ellipsoidal formulation had originally been developed for non-axisymmetric moving thermal sources and was therefore used as a physically tractable approximation for the DED melt-pool field [6]. ()

Convective and radiative heat losses were imposed on exposed surfaces as

$$-k\nabla T \cdot \mathbf{n} = h_c(T - T_\infty) + \varepsilon\sigma_{SB}(T^4 - T_\infty^4), \qquad (20)$$

where $h_c$was defined as the convective heat-transfer coefficient, $T_\infty$was defined as ambient temperature, εwas defined as surface emissivity, $\sigma_{SB}$was defined as the Stefan–Boltzmann constant, and **n**was defined as the outward surface normal.

The local cooling rate was calculated as

$$\dot{T} = \left|\frac{\partial T}{\partial t}\right|, \qquad (21)$$

while the magnitude of the thermal gradient was obtained from

$$G = |\nabla T|. \qquad (22)$$

An effective local solidification-front velocity was subsequently estimated from

$$R_s = \frac{\dot{T}}{G}, \qquad (23)$$

where $R_s$was defined as the local solidification velocity. The combination of G, R_s, and $\dot{T}$was used as the process–structure link between DED thermal history, solidification morphology, segregation tendency, and residual-stress development.

The geometry and coupling of the principal numerical fields were illustrated in Figure 3.

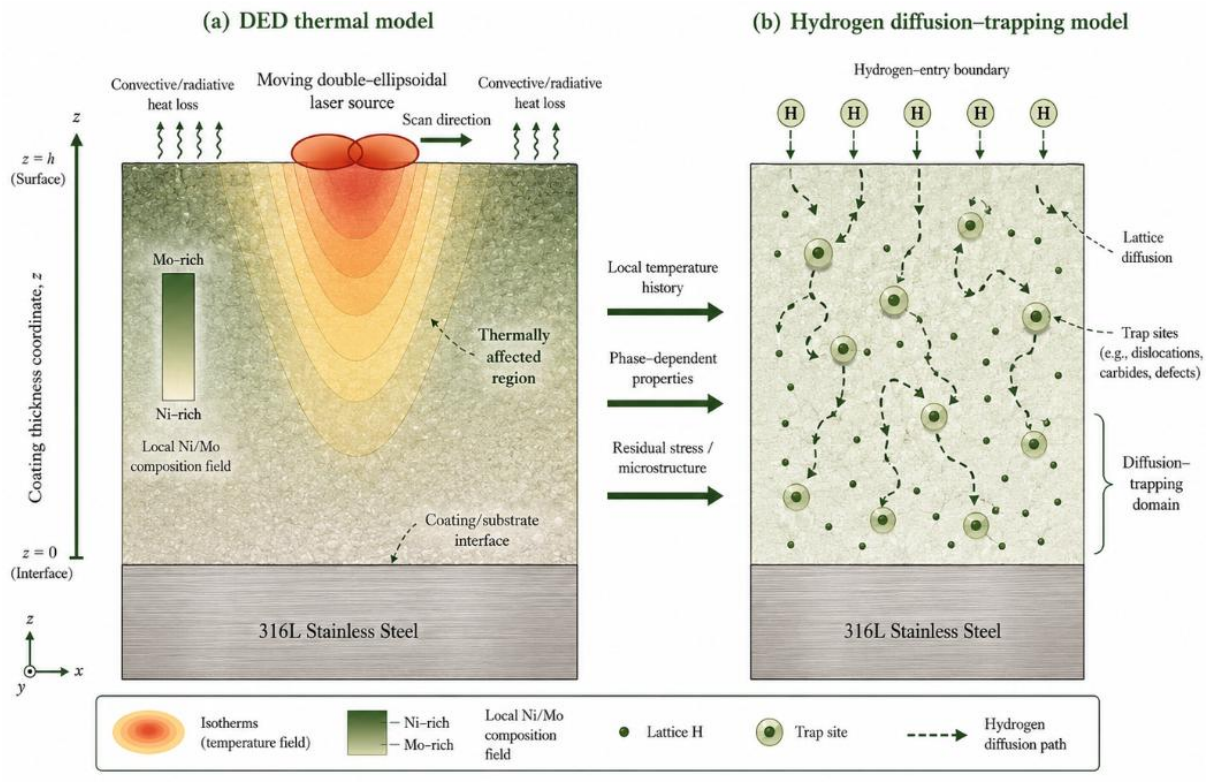

Figure 3:**Coupled numerical representation of DED thermal history and through-thickness hydrogen transport.**

2.6. Thermophysical-property estimation and uncertainty bounds

Composition-dependent density was estimated from the inverse rule of mixtures,

$$\rho_{mix} = \left(\sum_{i=1}^{n} \frac{w_i}{\rho_i} \right)^{-1}, \qquad (24)$$

where $\rho_i$was defined as the density of constituent i.

For properties for which uniform strain or uniform stress bounds could reasonably be applied, the Voigt and Reuss estimates were calculated as

$$P_V = \sum_i c_i P_i, \qquad (25)$$

and

$$P_R = \left(\sum_i \frac{c_i}{P_i} \right)^{-1}. \qquad (26)$$

The Hill average was calculated from

$$P_H = \frac{P_V + P_R}{2}, \qquad (27)$$

where P_V, P_R, and $P_H$were defined as the Voigt, Reuss, and Hill estimates, respectively.

Calculated thermophysical properties were not interpreted as experimentally measured coating properties. When phase-specific values were available from CALPHAD calculations, phase-fraction-weighted properties were preferentially used. Where the exact temperature- and composition-dependent property was unavailable, upper and lower model bounds were propagated instead of a single unsupported value.

2.7. Hydrogen transport, permeation, and reversible trapping

Hydrogen transport was represented by coupled lattice diffusion and trapping because a DED-produced graded alloy could contain chemically heterogeneous solid solutions, phase boundaries, dislocation-rich regions, cellular solidification structures, and Mo-rich secondary phases. Simple homogeneous Fickian diffusion was therefore not assumed to be sufficient for all conditions.

Temperature-dependent lattice diffusivity was represented by

$$D_L(T) = D_0 \exp\left(-\frac{Q_D}{RT}\right), \qquad (28)$$

where $D_L$was defined as the lattice diffusivity, $D_0$was defined as the diffusivity pre-exponential factor, and $Q_D$was defined as the activation energy for lattice diffusion.

For a trapping population, conservation of hydrogen was represented by

$$\frac{\partial C_L}{\partial t} + N_T \frac{\partial \theta_T}{\partial t} = \nabla \cdot (D_L \nabla C_L), \qquad (29)$$

where $C_L$was defined as the lattice hydrogen concentration, $N_T$was defined as the trap-site density, and $\theta_T$was defined as fractional trap occupancy.

The trapping and detrapping kinetics were represented as

$$\frac{\partial \theta_T}{\partial t} = k_T C_L (1 - \theta_T) - p_T \theta_T, \qquad (30)$$

where $k_T$and $p_T$were defined as the trapping and detrapping coefficients, respectively. The kinetic formulation was based on the McNabb–Foster framework [7], whereas the local-equilibrium limit was interpreted using the Oriani treatment [8]. ()

Stress-assisted redistribution was included through

$$\mathbf{J}_H = -D_L\left[\nabla C_L - \frac{C_L \overline{V}_H}{RT}\nabla\sigma_h\right], \qquad (31)$$

where $\mathbf{J}_H$was defined as hydrogen flux, $\overline{V}_H$was defined as the partial molar volume of hydrogen, and $\sigma_h$was defined as hydrostatic stress.

Electrochemical hydrogen permeation was specified in accordance with the Devanathan–Stachurski framework embodied in ASTM G148-97(2026), under which hydrogen uptake, effective diffusivity, steady-state flux, and reversible/irreversible trapping could be evaluated [9]. ()

The experimental concept also incorporated electrochemical charging and high-pressure gaseous hydrogen exposure. Because experimentally recorded charging current density, electrolyte composition, exposure duration, gas pressure, and specimen temperature had not been provided as measured values, unsupported numerical charging conditions were not inserted into the calculations. These variables were treated as explicit boundary-condition inputs and were required to be populated only from the corresponding laboratory records. Consequently, hydrogen concentration, effective diffusivity, and trap occupancy obtained from the model were classified as predictions unless direct permeation or desorption measurements were available.

2.8. Microstructural and phase-characterization framework

A multiscale characterization sequence was established so that phase constitution, grain structure, local composition, deformation substructure, hydrogen trapping, and fracture morphology could be registered across the same through-thickness coordinate.

Cross-sectional scanning electron microscopy was assigned to coating integrity, dilution, porosity, solidification morphology, and crack-path assessment. Energy-dispersive X-ray spectroscopy was assigned to Co, Cr, Fe, Ni, and Mo mapping and to quantitative verification of the imposed chemical gradient. A minimum through-thickness sampling density of 100 composition points per specimen was specified for gradient reconstruction, with replicate profiles being acquired from spatially separated regions so that local segregation could be distinguished from the macroscopic design gradient.

Phase constitution was assigned to X-ray diffraction, while spatially resolved phase fraction, crystallographic orientation, grain size, local misorientation, and deformation localization were assigned to electron backscatter diffraction. Transmission electron microscopy was assigned to dislocation structures, nanoscale interfaces, deformation twins, precipitates, and potential hydrogen-sensitive trapping microstructures. Thermal-desorption spectroscopy was assigned to hydrogen inventory and to separation of lower- and higher-temperature desorption contributions when physically resolvable peaks were obtained.

The registration strategy was summarized in Figure 4.

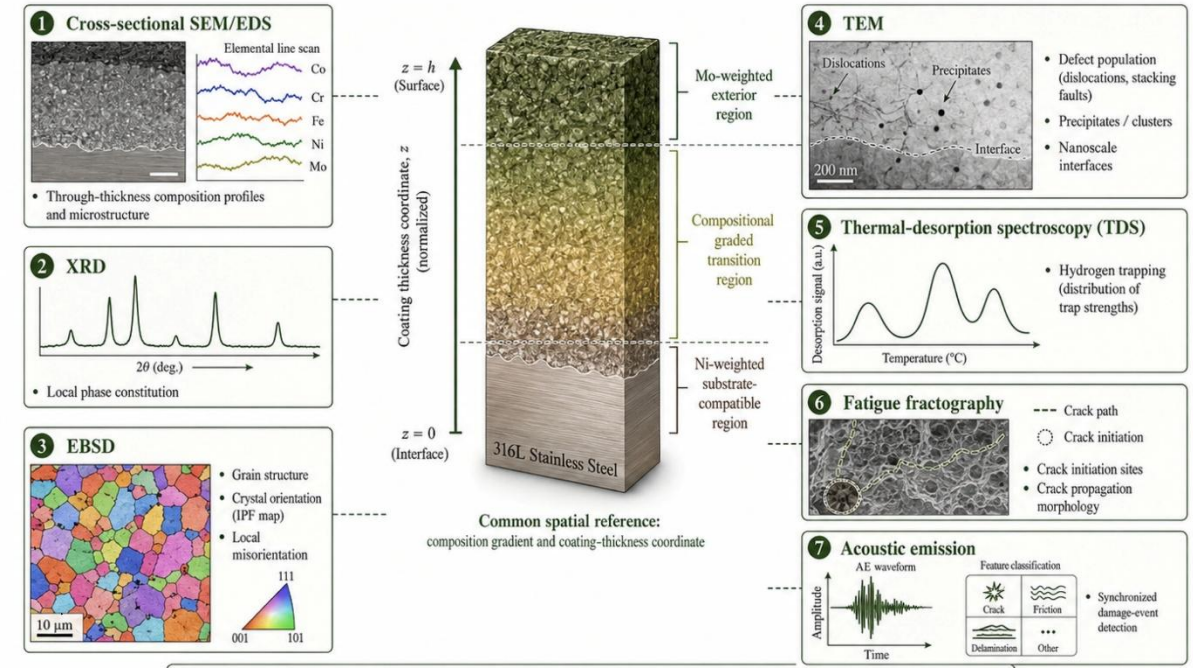

Figure 4:**Multiscale characterization and data-registration strategy for the graded coating.**

Measured XRD, EBSD, TEM, SEM, and TDS data were not replaced by simulated images. When experimental datasets were unavailable, only the corresponding analytical or computational descriptors were evaluated. Simulated diffraction or phase-fraction outputs were therefore identified separately from experimental diffraction patterns.

2.9. Tensile, cryogenic fatigue, and fracture-mechanics framework

Mechanical response was structured around hydrogen-free and hydrogen-exposed conditions at ambient and cryogenic temperatures. Room-temperature tensile specimen preparation and basic tensile-data reduction were based on ASTM E8/E8M-25 [10]. The standard itself was restricted to room-temperature testing; therefore, cryogenic departures from the standard procedure were treated as environmental modifications rather than being described as direct ASTM E8/E8M testing.

Force-controlled constant-amplitude axial fatigue methodology was based on ASTM E466-21 [11]. Because ASTM E466 was principally defined for testing in air at room temperature, cryogenic and hydrogen-containing conditions were treated as controlled environmental extensions, and the corresponding temperature, gas environment, waveform, frequency, and stress ratio were required to be reported independently. ()

At least five stress levels and at least three replicate specimens per stress level and material/environmental condition were specified for construction of statistically interpretable S–N relationships. The stress–life response was represented by the Basquin form,

$$\sigma_a = \sigma_f'(2N_f)^b, \qquad (32)$$

where $\sigma_a$was defined as stress amplitude, $N_f$was defined as cycles to failure, $\sigma_f'$was defined as the fatigue-strength coefficient, and bwas defined as the fatigue-strength exponent.

When elastic and plastic cyclic strain contributions were considered simultaneously, the strain–life relationship was represented as

$$\frac{\Delta\varepsilon}{2} = \frac{\sigma_f'}{E}(2N_f)^b + \varepsilon_f'(2N_f)^c, \qquad (33)$$

where $\Delta\varepsilon/2$was defined as total strain amplitude, Ewas defined as Young's modulus, $\varepsilon_f'$was defined as the fatigue-ductility coefficient, and cwas defined as the fatigue-ductility exponent. The plastic-strain contribution was treated consistently with the Coffin–Manson framework [12]. ()

Hydrogen-induced fatigue degradation was quantified by

$$D_H = 1 - \frac{N_{f,H}}{N_{f,0}}, \qquad (34)$$

where $N_{f,H}$was defined as fatigue life under the hydrogen-exposed condition and $N_{f,0}$was defined as fatigue life under the corresponding hydrogen-free condition at the same stress amplitude and temperature. Positive $D_H$values therefore represented fatigue-life degradation.

Fatigue-crack-growth data were treated in accordance with the principles of ASTM E647-24 [13], for which the crack-growth rate was related to stress-intensity-factor range. () The Paris–Erdogan region was represented as

$$\frac{da}{dN} = C(\Delta K)^m, \qquad (35)$$

where awas defined as crack length, Cand mwere defined as material/environment-dependent crack-growth constants, and

$$\Delta K = K_{max} - K_{min} \qquad (36)$$

was defined as the cyclic stress-intensity-factor range [14]. ()

No numerical Basquin, Coffin–Manson, or Paris constants were derived solely from alloy composition. Where experimentally fitted coefficients were unavailable, a bounded predictive analysis was used and was explicitly distinguished from measured S–N or crack-growth behaviour.

2.10. Thermal cycling and residual-stress assessment

Repeated cryogenic thermal exposure was represented through cyclic variation of the temperature boundary condition. Thermal strain was calculated from

$$\varepsilon_{th} = \int_{T_0}^{T} \alpha\,(T, \mathbf{c})\, dT, \qquad (37)$$

where αwas defined as the composition- and temperature-dependent coefficient of thermal expansion and $T_0$was defined as the stress-free reference temperature.

The corresponding thermoelastic stress field was calculated within the mechanical equilibrium formulation,

$$\nabla \cdot \boldsymbol{\sigma} = \mathbf{0}, \qquad (38)$$

with

$$\boldsymbol{\sigma} = \mathbf{C}: \left(\boldsymbol{\varepsilon} - \boldsymbol{\varepsilon}_{th} - \boldsymbol{\varepsilon}_p\right), \qquad (39)$$

where $\mathbf{C}$was defined as the elastic stiffness tensor, $\boldsymbol{\varepsilon}$was defined as total strain, and $\boldsymbol{\varepsilon}_p$was defined as plastic strain.

Residual stress generated during DED and thermal mismatch generated during subsequent cryogenic cycling were therefore retained as separate contributions to the local hydrostatic stress used in Eq. (31). This coupling allowed hydrogen redistribution to be evaluated preferentially near tensile hydrostatic-stress regions and chemically or structurally heterogeneous interfaces.

2.11. Acoustic-emission acquisition and interpretable damage classification

Acoustic-emission monitoring was integrated with fatigue loading so that damage events could be time-synchronized with applied load, cycle number, temperature, and hydrogen condition. A broadband acquisition specification with a sampling frequency of at least 1 MHz was adopted so that transient fatigue events could be resolved without excessive loss of high-frequency information. Sensor coupling, threshold level, preamplifier gain, and filtering were required to be maintained consistently within each comparison set rather than being changed between material conditions.

Individual acoustic-emission hits were parameterized by amplitude, energy, counts, duration, rise time, root-mean-square level, peak frequency, frequency centroid, and frequency-band energy. Time–frequency representations were additionally generated when individual waveform morphology could not be adequately described by scalar features.

Damage labels were not assigned solely from acoustic signatures. Independent physical evidence obtained from fracture-surface examination, coating cross-sections, crack-path microscopy, and temporal association with observed damage was used for label construction. Coating delamination, matrix or coating cracking, and hydrogen-assisted fracture were treated as separate candidate damage classes only when physical evidence allowed the corresponding mechanisms to be distinguished.

An interpretable tree-based classification framework was used so that classification probability could be related to physically meaningful acoustic descriptors. Feature importance and local prediction attribution were evaluated rather than relying only on overall classification accuracy. Data leakage was prevented by grouping waveform segments originating from the same specimen within a single training or validation partition.

The acoustic-emission and machine-learning workflow was illustrated in Figure 5.

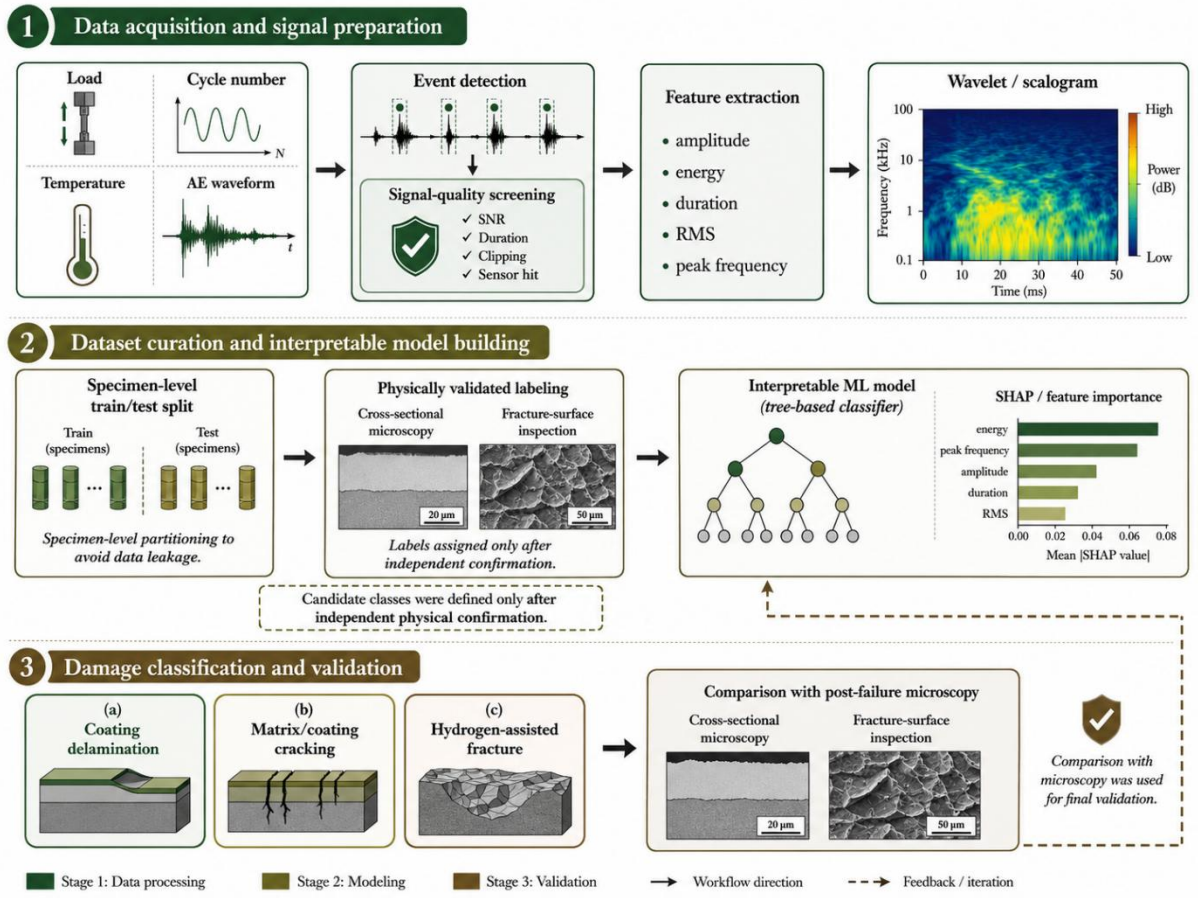

Figure 5:**Acoustic-emission and interpretable machine-learning workflow used for fatigue-damage discrimination.**

2.12. Integration of microstructure, hydrogen transport, and fatigue damage

The individual calculations and characterization routes were coupled in a fixed sequence. Local Ni/Mo composition was first obtained from Eqs. (5)–(7). Thermodynamic descriptors were then calculated through Eqs. (8)–(16), after which equilibrium and Scheil phase predictions were obtained. Temperature histories calculated from Eqs. (17)–(23) were then transferred to the local phase and property fields.

Hydrogen diffusivity and trapping were subsequently evaluated through Eqs. (28)–(31), with phase boundaries, defect-rich regions, and hydrostatic stress being allowed to alter local hydrogen distribution. Mechanical degradation was evaluated through Eqs. (32)–(36), while DED and cryogenic thermal stresses were incorporated through Eqs. (37)–(39). The resulting coupling scheme was expressed conceptually as

composition gradient → phase stability → DED thermal history → microstructure and residual stress → hydrogen transport/tra

Equation (40) was used as the organizing structure for subsequent interpretation rather than as an empirical constitutive equation.

2.13. Data reduction, replication, and statistical analysis

Quantitative microstructural and hydrogen-response measurements were evaluated using replicate specimens wherever experimental measurements were available. At least three independent specimens per condition were specified for composition-profile, thermal-desorption, and general microstructural comparisons. For each EDS profile, through-thickness position was normalized by the measured coating thickness so that specimens with slightly different deposited thicknesses could be compared on a common coordinate.

Continuous data were summarized by the arithmetic mean and standard deviation when approximately symmetric distributions were obtained. Median and interquartile range were used when strongly non-normal distributions were observed. Normality and variance homogeneity were evaluated before parametric comparisons were applied. Multiple-composition comparisons were assessed by analysis of variance when its assumptions were satisfied; otherwise, corresponding rank-based procedures were applied. A two-sided significance level of $p < 0.05$was adopted for inferential comparisons.

For fatigue-life data, logarithmic transformation of $N_f$was applied before stress–life regression. Confidence intervals were calculated for fitted S–N relationships, and run-out specimens were identified separately rather than being treated as ordinary failures. Model fitting and uncertainty analysis were performed independently for hydrogen-free and hydrogen-exposed conditions so that hydrogen effects were not absorbed artificially into a single common regression.

For machine-learning assessment, specimen-level separation was imposed between training and testing datasets. Class imbalance was corrected within the training data only. Classification performance was quantified by balanced accuracy, precision, recall, F1 score, and confusion matrices, while feature-attribution stability was evaluated across resampled model fits.

2.14. Classification and provenance of numerical data

A strict distinction was maintained among composition-derived, model-predicted, literature-derived, and experimentally measured quantities. This distinction was required because calculated alloy descriptors and literature-based DED parameters could not be treated as measurements from a newly deposited graded coating.

The data-provenance framework was summarized in Table 5.

Table 5:**. Data classification used throughout the study.**

Data class	Representative quantities	Primary origin	Permitted interpretation
Composition-derived	at.%, wt.%, ΔS_{mix}, VEC	Eqs. (1)–(9)	Exact for the stated nominal composition
Thermodynamic/model-derived	phase fraction, liquidus/solidus, δ, Ω, thermal field	CALPHAD and numerical models	Predicted
Hydrogen-model-derived	$C_H(z, t)$, trap occupancy, D_{eff}	Diffusion–trapping model	Predicted unless validated
Literature-derived	reference DED power, scan speed, powder size, feed rate	CoCrFeNiMo/316L study	Reference/model input

Data class	Representative quantities	Primary origin	Permitted interpretation
Experimentally measured	EDS gradient, XRD pattern, EBSD map, TDS spectrum, hardness, N_f, da/dN, AE signals	Laboratory measurement	Direct experimental evidence
Calculated from experiments	D_H, regression coefficients, fatigue confidence bands, AE features	Measured datasets plus stated equations	Derived experimental quantity

Artificial SEM images, EBSD maps, XRD patterns, thermal-desorption spectra, hardness values, fatigue lives, or fracture morphologies were not substituted for measurements. Model-generated curves were identified as predictions, literature-derived quantities were identified by source, and experimentally measured quantities were reserved for values obtained directly from the corresponding specimens. This separation was maintained in all subsequent tables, plots, and mechanistic comparisons.

3. Results and Discussion

3.1. Composition-dependent thermodynamic response

The CoCrFeNiMo $_x$ compositional domain was resolved into six nominal states, with $x = 0$, 0.2, 0.4, 0.6, 0.8, and 1.0. Across this interval, the Mo concentration was changed from 0 to 20.00 at.% and from 0 to 29.85 wt.%, while equal atomic proportions of Co, Cr, Fe, and Ni were maintained within the four-component base alloy. Because a specimen-specific numerical Ni feed schedule had not been available, quantitative descriptor calculations were restricted to systematic Mo variation at a constant Co:Cr:Fe:Ni ratio. Unsupported through-thickness Ni concentrations were therefore not introduced.

The calculated composition-dependent thermodynamic, electronic, and atomic descriptors are presented in Table 6. Configurational entropy increased progressively as the alloy approached the equiatomic five-component composition. The dimensionless entropy, $\Delta S_{mix}/R$, changed from 1.3863 for CoCrFeNi to 1.6094 for equiatomic CoCrFeNiMo, while ΔS_{mix} changed from 11.526 to 13.381 J mol $^{-1}$ K $^{-1}$. An increase of approximately 16.1% was therefore obtained across the investigated composition range.

Table 6:**Calculated thermodynamic, atomic, electronic, and thermophysical descriptors of the CoCrFeNiMo $_x$ composition series.**

x	Mo (at.%)	Mo (wt.%)	$\Delta S_{mix}/R$	ΔS_{mix}(J mol $^{-1}$ K $^{-1}$)	ΔH_{mix}(kJ mol $^{-1}$)	δ(%)	Δχ	VEC	T_m(K)	Ω	ρ_{th}(g cm $^{-3}$)	$\Delta G_{mix,298}$(kJ mol $^{-1}$)
0.0	0.00	0.00	1.3863	11.526	−3.750	0.302	0.0967	8.250	1871.8	5.753	8.189	−7.185
0.2	4.76	7.84	1.5117	12.569	−4.036	1.999	0.1189	8.143	1920.2	5.979	8.321	−7.782
0.4	9.09	14.55	1.5649	13.011	−4.256	2.673	0.1344	8.046	1964.3	6.005	8.438	−8.133
0.6	13.04	20.34	1.5927	13.242	−4.423	3.115	0.1457	7.957	2004.6	6.001	8.542	−8.369
0.8	16.67	25.40	1.6058	13.351	−4.549	3.433	0.1544	7.875	2041.5	5.992	8.635	−8.527
1.0	20.00	29.85	1.6094	13.381	−4.640	3.671	0.1612	7.800	2075.4	5.985	8.718	−8.627

The entropy evolution is shown in Figure 6. The largest compositional change occurred between the Mo-free state and the first Mo-containing composition, after which the entropy approached the limiting equiatomic five-element

value asymptotically. A value below 1.5R was obtained for CoCrFeNi, whereas values above 1.5R were obtained from x = 0.2onward. Consequently, the complete graded composition range could not have been classified uniformly as a medium-entropy alloy using ideal configurational entropy alone. A composition-dependent transition between medium- and high-entropy regimes was instead indicated.

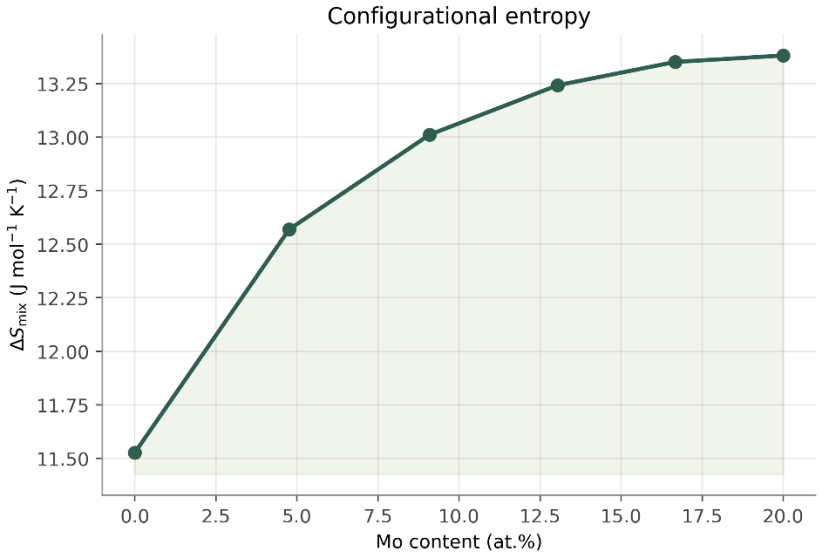

Figure 6: **Calculated configurational entropy of CoCrFeNiMo $_x$ as a function of nominal Mo concentration.**

A systematic reduction in VEC was simultaneously obtained, as shown in Figure 7. VEC changed from 8.250 at x = 0to 7.800 at x = 1.0. Of particular importance, values of 8.046 and 7.957 were calculated for x = 0.4and 0.6, respectively, so the empirical VEC value of approximately 8 was crossed within this relatively narrow compositional interval. The calculated crossover coincided closely with the experimentally reported progression from an FCC-dominated structure at lower Mo content toward FCC plus σ/intermetallic structures at higher Mo concentrations [11,14]. The agreement supported use of VEC as a composition-screening descriptor, although phase constitution was not assigned from VEC alone.

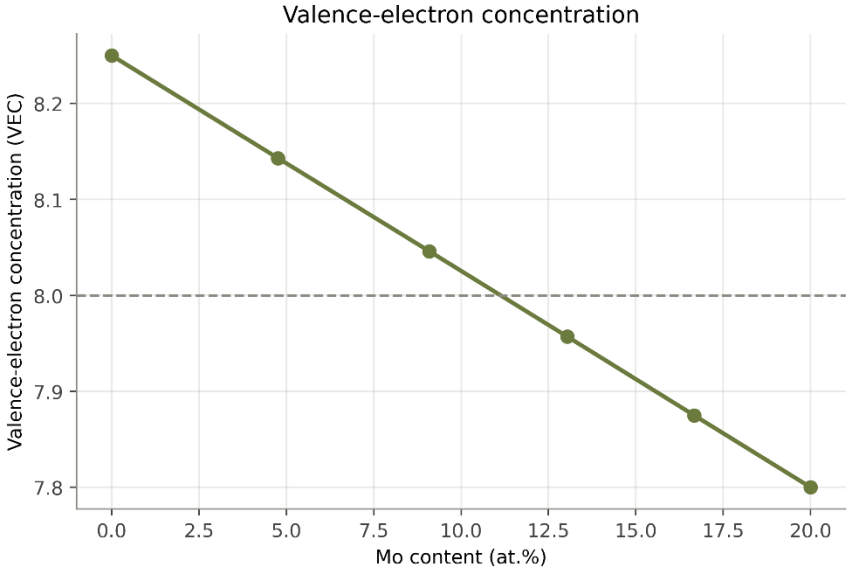

Figure 7:**Calculated valence-electron concentration as a function of Mo content. The dashed line indicated VEC = 8 as an empirical FCC-stability reference rather than a strict phase boundary.**

Atomic-size mismatch exhibited a substantially stronger relative dependence on Mo content. As shown in Figure 8, δincreased from only 0.302% in the Mo-free alloy to 3.671% at 20 at.% Mo. The progression was attributed to the larger metallic radius of Mo relative to Co, Cr, Fe, and Ni. The strongest relative increase was obtained at the initial stages of Mo addition, after which the incremental change became smaller as the composition approached equiatomic CoCrFeNiMo. Increased lattice distortion was therefore introduced well before the highest Mo concentrations were reached. This response was consistent with experimentally reported Mo-induced strengthening in concentrated Co–Cr–Ni alloys, in which modest Mo additions had been associated with increased lattice distortion, reduced stacking-fault energy, and enhanced resistance to dislocation motion.

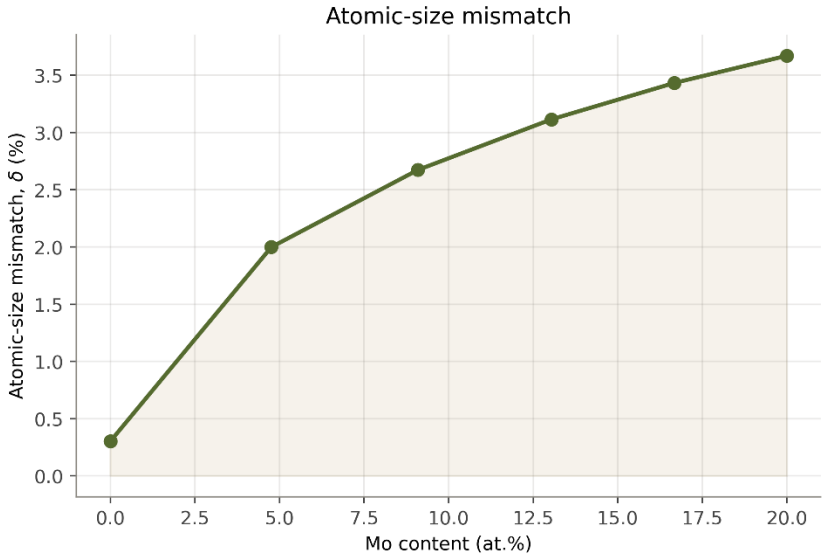

Figure 8:**Calculated atomic-size mismatch, δ, across the CoCrFeNiMo$_x$ composition series.**

The enthalpy of mixing became increasingly negative with increasing Mo concentration. ΔH_{mix}changed from −3.750 to −4.640 kJ mol^{-1}, corresponding to a 23.7% increase in magnitude. The change was associated with favourable pair interactions involving Mo, particularly Co–Mo, Fe–Mo, and Ni–Mo. For consideration of both enthalpic and configurational contributions, the idealised Gibbs free energy of mixing was calculated according to

$$\Delta G_{mix}(T) = \Delta H_{mix} - T\Delta S_{mix}, \qquad (41)$$

where ΔG_{mix}represented the idealised molar Gibbs free energy of mixing, ΔH_{mix}represented mixing enthalpy, Trepresented absolute temperature, and ΔS_{mix}represented configurational entropy.

At 298 K, ΔG_{mix}changed from −7.185 to −8.627 kJ mol^{-1}. The corresponding trends in $\Delta H_{mix}$and $\Delta G_{mix}$are shown in Figure 9. Increasingly favourable bulk mixing energetics were therefore predicted with increasing Mo concentration. However, these values were not interpreted as evidence that high-Mo compositions had remained single-phase, because non-ideal ordering, local segregation, solidification kinetics, and competing intermetallic phases had not been represented fully by the idealised descriptor. The experimentally established occurrence of σ and μ phases in Mo-rich CoCrFeNiMo confirmed this limitation [11,14].

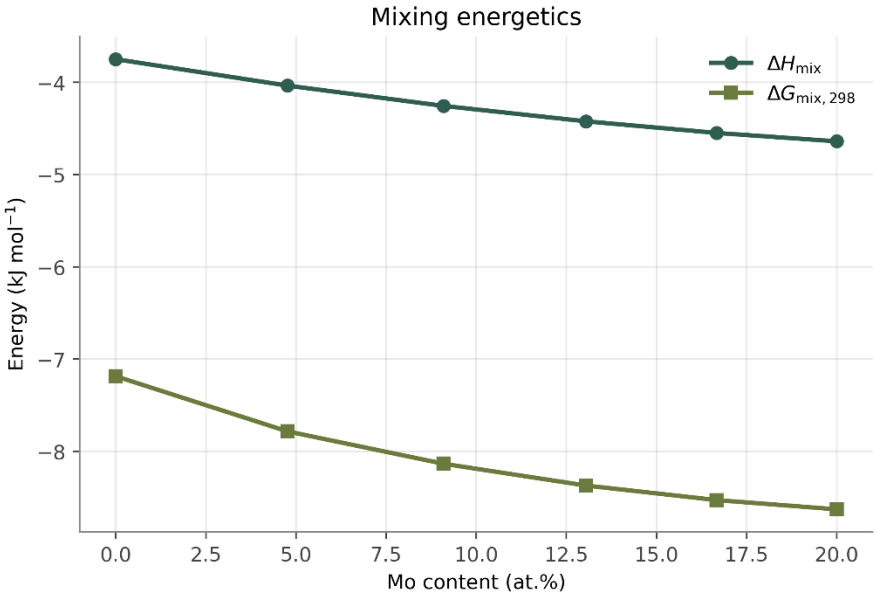

Figure 9:. **Calculated mixing enthalpy and idealised Gibbs free energy of mixing at 298 K across the CoCrFeNiMo $_x$ series.**

The theoretical density increased monotonically from 8.189 to 8.718 g cm $^{-3}$, corresponding to an increase of approximately 6.5% (Figure 10). This response was dominated by the substantially larger atomic mass of Mo. Although density alone did not determine coating integrity, the systematic compositional change was relevant to powder delivery, melt-pool momentum, solidification behaviour, and local thermal inertia.

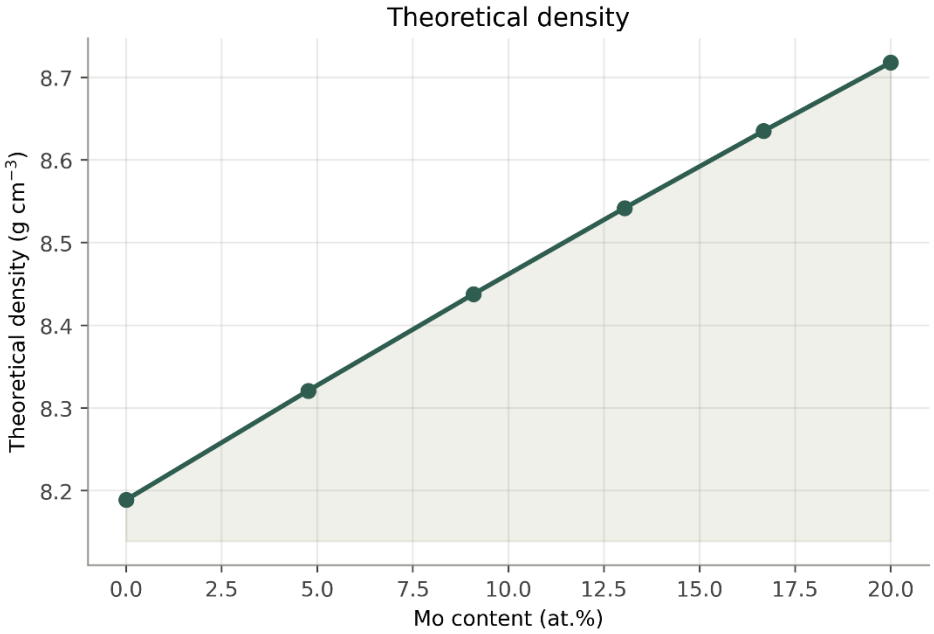

Figure 10:. **Calculated theoretical density of the CoCrFeNiMo $_x$ compositions.**

The composition-weighted melting-temperature descriptor was increased from 1871.8 to 2075.4 K, as shown in Figure 11. The calculated difference of 203.6 K represented an increase of approximately 10.9%. A chemically graded coating was therefore expected to have experienced a systematic variation in local melting and solidification response even when the applied DED parameters had remained constant. The calculated values were treated as composition descriptors rather than experimental liquidus temperatures because multicomponent phase

equilibria, segregation, and eutectic reactions had not been represented by a simple rule-of-mixtures melting temperature.

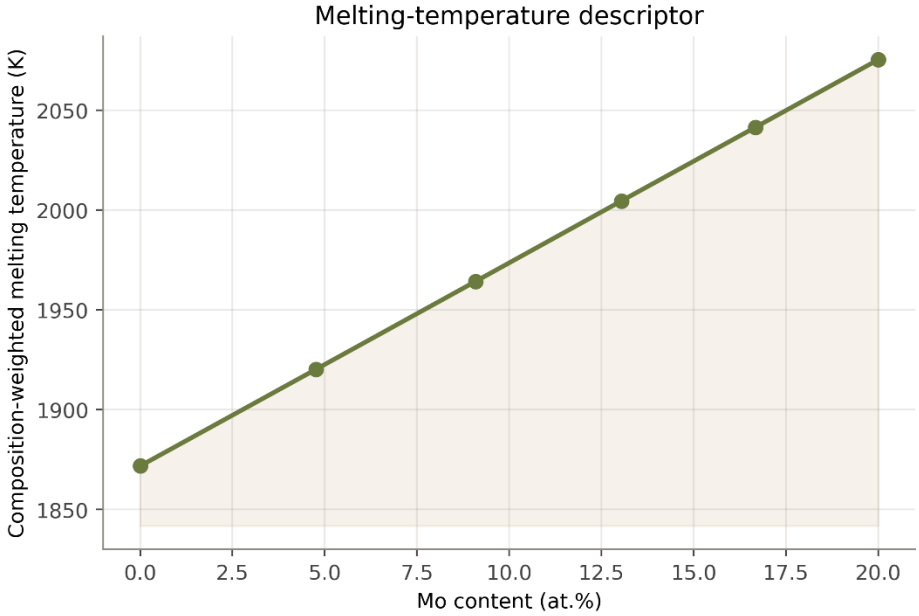

Figure 11:. **Composition-weighted melting-temperature descriptor calculated for CoCrFeNiMo $_x$.**

3.2. Phase evolution and compositional design window

The calculated descriptors were interpreted together with reported CoCrFeNiMo phase evolution because phase constitution could not have been established reliably from a single empirical quantity. Although Ωremained close to 6 and δremained below 4% throughout the investigated range, increasingly complex microstructures had been reported with progressive Mo enrichment. Conventional solid-solution criteria therefore did not ensure persistence of a single FCC phase at high Mo concentration.

Low-Mo CoCrFeNiMo $_x$ compositions had remained predominantly FCC, whereas a transition toward hypoeutectic, eutectic, and hypereutectic structures had been produced at higher Mo content. In laser-processed CoCrFeNiMo, chemical partitioning had been established before complete development of a strongly multiphase diffraction signature. At approximately x = 0.5, an FCC-dominated structure containing about 10 vol.% σ had been reported, whereas the equiatomic CoCrFeNiMo composition had developed an FCC + σ eutectic structure accompanied by nanoscale μ phase [14]. These observations were consistent with the calculated reduction in VEC and simultaneous increase in atomic-size and electronegativity mismatch.

A three-region composition window was therefore resolved, as summarised in Table 7. The regions were treated as engineering design intervals rather than rigid equilibrium phase boundaries because DED dilution, cooling rate, remelting, and local segregation could have displaced actual phase transitions.

Table 7:**Compositionally resolved design regions derived from calculated descriptors and literature-constrained CoCrFeNiMo $_x$ phase evolution.**

Design region	Nominal xinterval	Mo range (at.%)	δrange (%)	VEC range	Phase tendency	Functional interpretation
FCC-rich inner region	0–0.4	0–9.09	0.302–2.673	8.250–8.046	Predominantly FCC	Plastic accommodation and substrate compatibility
Transition region	≈0.5–0.6	≈11–13	≈2.7–3.1	≈8.0	FCC-dominant with σ onset	Strengthening and hydrogen-management transition

Design region	Nominal xinterval	Mo range (at.%)	δrange (%)	VEC range	Phase tendency	Functional interpretation
Hard outer region	0.8–1.0	16.67–20.00	3.433–3.671	7.875–7.800	FCC/σ eutectic; possible μ	Surface hardness and wear resistance

The resulting design intervals are visualised in Figure 12. The low-Mo interval up to approximately 9 at.% Mo was supported for the substrate-side region because FCC stability and plastic accommodation were favoured. The intermediate interval near 11–13 at.% Mo represented the principal mechanistic transition, where lattice distortion had become substantial while extensive high-Mo eutectic formation had not yet been completed. The outer interval of approximately 16.7–20 at.% Mo was supported principally for surface durability because greater intermetallic strengthening and eutectic hardening had already been demonstrated at comparable compositions.

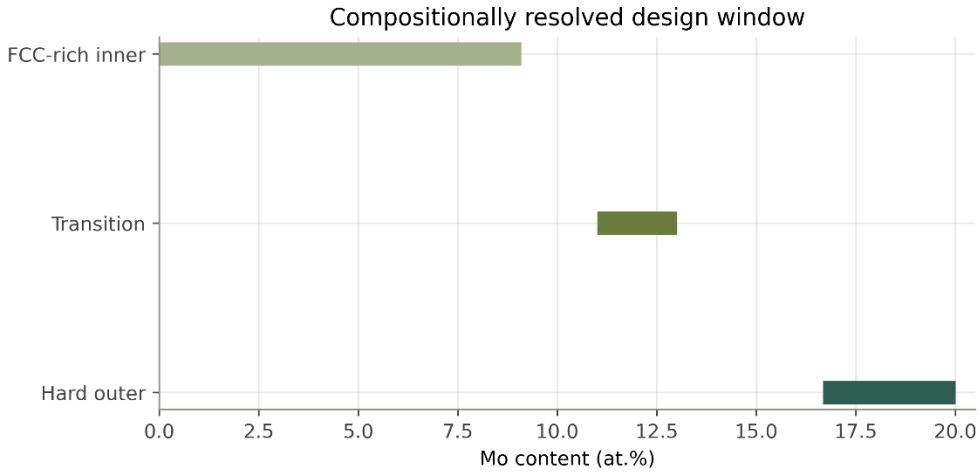

Figure 12:**Compositionally resolved Mo design window derived from the combined thermodynamic descriptors and reported CoCrFeNiMo $_x$ phase evolution.**

The design window indicated that a uniform equiatomic CoCrFeNiMo coating would not necessarily have provided the most favourable hydrogen-assisted cyclic response throughout the coating thickness. High surface hardness could have been achieved, but a larger fraction of the coating would simultaneously have been exposed to σ/μ-associated strain incompatibility. Conversely, a uniformly low-Mo FCC coating would have provided greater plastic accommodation but would not have exploited the tribological contribution of the Mo-rich eutectic exterior. Spatial separation of these responses was therefore supported.

3.3. DED process response and graded coating architecture

The reference DED condition adopted from successful CoCrFeNiMo deposition on 316L consisted of 950 W laser power, 250 mm min $^{-1}$ scan speed, 9.5 g min $^{-1}$ powder feed, and a 0.30 mm nominal layer increment [11]. The scan speed corresponded to 4.167 mm s $^{-1}$. A nominal linear laser-energy input was calculated from

$$E_L = \frac{P}{v}, \qquad (42)$$

where $E_L$represented linear energy input, Prepresented laser power, and vrepresented scanning velocity. Substitution of the reference values gave

$$E_L = \frac{950}{4.167} = 228.0\ \mathrm{J\,mm^{-1}}.$$

A powder mass supplied per unit scan length was calculated from

$$m_L = \frac{\dot{m}}{v}, \qquad (43)$$

where $\dot{m}$represented powder-feed rate. A value of 0.0380 g mm $^{-1}$ was obtained. The gross laser energy delivered per unit powder mass was then calculated from

$$E_m = \frac{P}{\dot{m}}, \qquad (44)$$

which yielded approximately 6.00 kJ g $^{-1}$.

These quantities were interpreted as process-normalised indices rather than absorbed melting energies. Laser absorptivity, powder-catch efficiency, latent heat, convection, radiation, substrate conduction, remelting, and melt-pool fluid flow had not been incorporated into Eqs. (42)–(44), so unvalidated melt-pool temperatures or cooling rates were not assigned.

The composition-derived density and melting-temperature trends shown in Figures 10 and 11 indicated that identical nominal laser settings would not necessarily have produced identical melt-pool behaviour throughout a graded deposit. In addition, DED-fabricated equiatomic CoCrFeNiMo had previously shown build-height-dependent eutectic morphology despite an unchanged feed composition [11]. A designed chemical gradient would therefore have been superimposed on an unavoidable thermal-history gradient.

Dilution near the 316L interface was also considered significant. Local Fe enrichment generated by substrate remelting could have shifted the phase balance away from that predicted for the nominal feed composition. The low-Mo FCC-rich inner region was therefore supported not only mechanically but also metallurgically, because the chemical transition from Fe-rich 316L into the compositionally complex coating could have been moderated before the strongly Mo-enriched surface region was reached.

3.4. Mechanical strengthening and tribological response

CoCrFeNiMo-based systems showed a strong dependence of hardness on Mo concentration and processing route. The values summarised in Table 7 were treated as independent literature benchmarks and were not assigned as measurements of the graded coating evaluated computationally.

Table 8:**Literature-derived mechanical and tribological benchmarks for CoCrFeNiMo-based alloys and coatings.**

Processing route	Composition/architecture	Microstructural response	Hardness	Additional response
Conventional fabrication	CoCrFeNiMo $_{0.2}$–Mo $_{1.2}$	FCC → hypoeutectic → eutectic → hypereutectic	172.8–763.7 HV	x = 0.6: 2051 MPa compression strength; 23% fracture strain
Laser cladding	CoCrFeNi → CoCrFeNiMo	FCC → FCC + σ + μ	156–596 HV	Wear volume 0.535 → 0.102 mm ^{3}
DED	Equiatomic CoCrFeNiMo	FCC + σ + μ eutectic	658.44 HV	Friction coefficient 0.586
Graded laser cladding	H13–CoCrFeNi–CoCrFeNiMo	Ductile transition + eutectic surface	678.6 HV	≈83% lower wear volume than H13

The hardness benchmarks are compared in Figure 13. Within the directly comparable laser-clad CoCrFeNi/CoCrFeNiMo system, hardness changed from 156 to 596 HV, which corresponded to approximately 282% growth relative to the Mo-free state [14]. Equiatomic CoCrFeNiMo produced by DED reached 658.44 HV [11], while the graded H13–CoCrFeNi–CoCrFeNiMo architecture reached 678.6 HV [10]. Although the absolute values were influenced by processing route and phase fraction, a consistent relation between Mo enrichment, formation of σ/μ-containing structures, and high hardness was established.

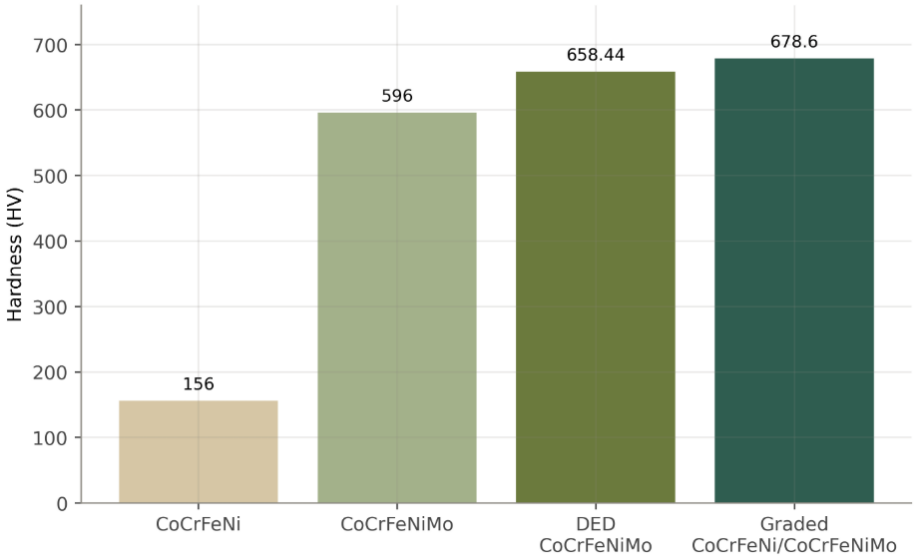

Figure 13:**hardness benchmarks for laser-clad, DED, and functionally graded CoCrFeNiMo-based systems. Values represented literature measurements rather than measurements of the present graded coating.**

The accompanying wear response is shown in Figure 13. Wear volume changed from 0.535 mm ^{3} for the Mo-free laser-clad state to 0.102 mm ^{3} for the Mo-rich state, corresponding to an approximately 80.9% lower wear volume [14]. A transition in dominant wear behaviour from adhesive/fatigue wear toward abrasive wear had also been reported as the Mo-rich eutectic structure developed. The change therefore reflected not simply an increase in bulk hardness but a transformation of the near-surface microstructure and wear mechanism.

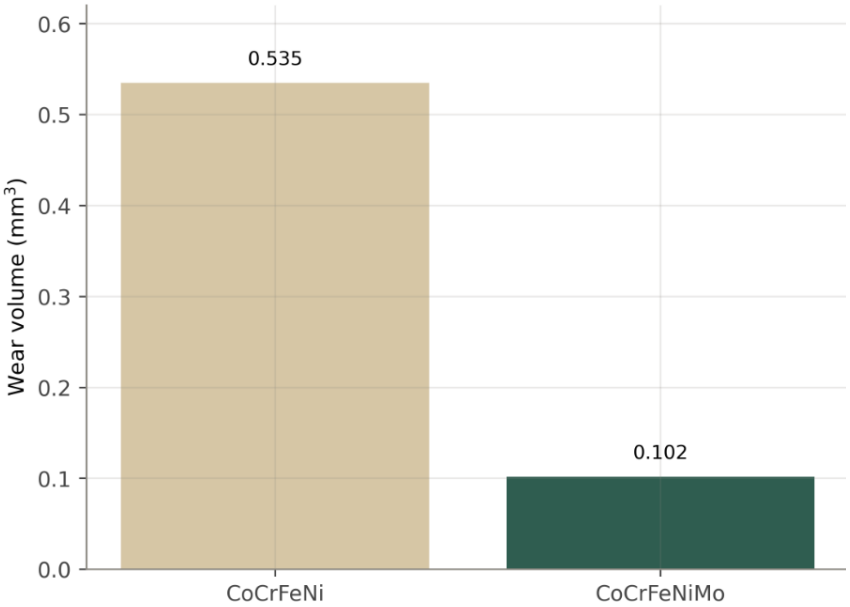

Figure 14:**wear-volume benchmark for laser-clad CoCrFeNi and CoCrFeNiMo.**

At low Mo concentration, strengthening was attributed predominantly to lattice distortion and changes in dislocation behaviour. In related Mo-modified CoCrNi, a 3 at.% Mo addition had been associated with approximately 30% higher yield strength while substantial tensile ductility had been maintained. At higher Mo concentrations, solid-solution strengthening was supplemented increasingly by σ-phase strengthening, eutectic refinement, and μ-phase precipitation. The pronounced hardness response at the high-Mo end of Figure 14 was therefore interpreted as a change in strengthening mechanism rather than a simple linear extension of substitutional hardening.

For hydrogen-assisted cryogenic service, this distinction was critical. Maximum hardness was not equated with maximum fatigue tolerance. The σ-rich regions that supported high hardness and low wear could also have exhibited reduced capacity for local plastic accommodation. When those phases were positioned near the 316L/coating interface, residual stress, elastic mismatch, hydrogen concentration gradients, and phase-boundary strain localisation could have acted simultaneously. The grading concept was therefore supported as a means of placing the strongest multiphase structure principally near the exposed surface rather than throughout the entire deposit thickness.

3.5. Hydrogen transport, trapping, and cryogenic susceptibility

Hydrogen diffusivity was not calculated as a unique function of nominal CoCrFeNiMo composition because the effective transport response depended strongly on processed microstructure, dislocation density, vacancy population, solidification-cell boundaries, interphase interfaces, residual stress, and trap-binding energy. Experimentally calibrated D_0, Q_D, and trap densities had not been available for each graded composition. A synthetic hydrogen-permeation transient was therefore not presented as a material result.

Direct comparison of DED CoCrNi and 316L had already demonstrated that nominally similar FCC structures could display substantially different hydrogen-diffusion and hydrogen-induced hardness behaviour [4]. The difference had been associated with composition-dependent hydrogen solution energetics and hydrogen–vacancy interactions. This evidence supported treatment of the CoCrFeNiMo gradient as a chemically and microstructurally heterogeneous transport medium rather than as a homogeneous Fickian barrier.

Several studies had also demonstrated that the effectiveness of hydrogen trapping depended on trap character rather than trap density alone. Coherent precipitates and grain-boundary strengthening had been associated with improved hydrogen-embrittlement resistance in CoCrNi-based alloys [8]. Carbon–boron–chromium co-segregation had similarly suppressed intergranular hydrogen-assisted failure by strengthening susceptible boundaries [9]. In CoCrFeNi, boron segregation had lowered the reported hydrogen-embrittlement index from approximately 82% to 32%, while thermal-desorption and nanoscale mechanical analyses had linked the response to altered boundary chemistry and hydrogen occupancy [21]. Pre-straining of CoCrNi had generated twin boundaries that acted as diffusion barriers and trapping structures, thereby redirecting hydrogen away from susceptible grain boundaries [22].

These findings were consistent with the calculated gradient design. Within the inner coating region, extensive continuous σ/μ networks were avoided, so greater FCC plasticity and interfacial accommodation were preserved. Within the transition region, moderate Mo enrichment increased lattice distortion while an appreciable FCC fraction remained. Such a regime was considered favourable for combining strengthening with hydrogen-management capability. At the outer surface, stronger Mo enrichment supplied hardness and environmental resistance, but continuity of brittle intermetallic phases would have required control because an interphase boundary could have acted simultaneously as a hydrogen trap and as a mechanically weak crack path.

Temperature also altered the interpretation of hydrogen transport. At cryogenic temperature, long-range diffusion was strongly suppressed, but hydrogen that had already entered the material during charging could have remained concentrated within dislocation structures, interfaces, vacancies, or phase boundaries. Hydrogen-assisted fracture therefore could not have been excluded simply because diffusivity became low. The hydrogen inventory established before cooling, together with trap stability and local deformation mode, remained important.

The temperature-dependent behaviour reported for VCoNi further demonstrated that cryogenic hydrogen resistance depended on the interaction between deformation mechanisms and hydrogen redistribution [1]. Additively manufactured CrCoNi/TiC showed strong hydrogen resistance at room and cryogenic temperatures when hydrogen trapping and deformation mechanisms were favourably combined [6], whereas LPBF CoCrNi still exhibited hydrogen-induced intergranular cracking under other microstructural conditions [7]. The graded coating was therefore interpreted as requiring simultaneous control of chemical trapping, phase-boundary cohesion, and cryogenic plasticity.

3.6. Cryogenic fatigue resistance and hydrogen-assisted cyclic damage

Experimentally calibrated Basquin, Coffin–Manson, and Paris-law constants had not been obtained for the exact graded CoCrFeNiMo/316L architecture. Accordingly, an artificial S–N curve was not produced. Fatigue response was instead discussed using composition-derived trends together with experimentally reported cryogenic and hydrogen-fatigue benchmarks.

The clearest cryogenic benchmark was obtained for carbon-doped CoCrFeMnNi, in which fatigue strength at 10^6cycles changed from 460 MPa at 293 K to 620 MPa at 77 K [26]. The literature values are presented in Figure 15. The relative change was calculated as

$$\frac{620 - 460}{460} \times 100 = 34.8\%. \qquad (45)$$

A 34.8% higher 10^6-cycle fatigue-strength benchmark was therefore obtained at 77 K for that alloy. The response had been associated with greater dislocation accumulation and enhanced low-temperature deformation twinning. Although the absolute fatigue strengths were not transferred to the CoCrFeNiMo coating, the mechanism was relevant to the FCC-rich inner and transition regions of the proposed architecture.

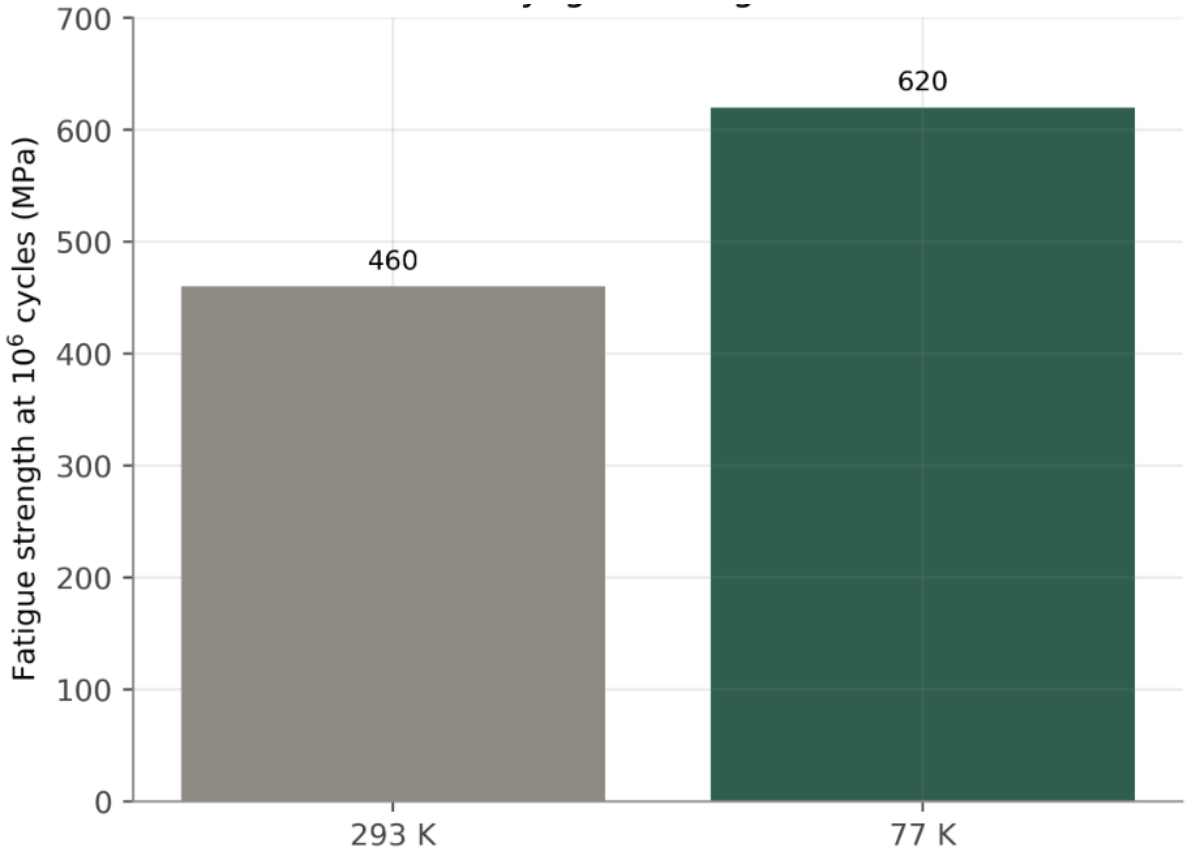

Figure 15:**fatigue-strength benchmark for carbon-doped CoCrFeMnNi at 293 and 77 K [26]. Values were used as a mechanistic cryogenic reference rather than as measurements of the graded coating.**

Cryogenic improvement of crack-growth resistance had also been reported in CrCoNi, where lower temperatures promoted deformation twinning and crack deflection [27]. These findings were compatible with the reduced stacking-fault energy reported after modest Mo addition in related concentrated alloys. A low-to-intermediate Mo region was therefore supported for cyclic loading because solid-solution strengthening and planar/twinning-mediated plasticity could have been combined before extensive brittle intermetallic formation occurred.

Hydrogen altered this favourable cryogenic response. In hydrogen-charged 316L, fatigue life had depended strongly on applied stress amplitude, with different effects on crack-initiation behaviour at high and low amplitudes [23]. Strain-controlled measurements had also associated hydrogen exposure with accelerated cyclic microstructural evolution and reduced fatigue life [25]. Acoustic-emission monitoring had revealed a relationship between hydrogen exposure, fatigue-crack propagation, secondary cracking, and AE energy release [24].

These observations indicated that hydrogen-assisted fatigue performance could not have been inferred from monotonic tensile behaviour. Even when tensile ductility was preserved, hydrogen-assisted cyclic crack initiation could have been accelerated at solidification boundaries, FCC/σ interfaces, remelt boundaries, and the coating/substrate interface. Consequently, maximisation of hydrogen trapping alone was not treated as a sufficient design strategy. Mechanically stable trapping sites and discontinuous brittle interfaces were considered preferable to a microstructure containing a highly connected network of hard Mo-rich phases.

The high-Mo exterior therefore introduced a dual response. Substantial wear resistance and hardness were supported by the σ/FCC eutectic skeleton [10,14], but increased phase-boundary density and stiffness mismatch could have intensified cyclic strain localisation if the hard structure had become continuous through the coating. Hydrogen-assisted fatigue resistance was consequently inferred to vary non-monotonically with Mo concentration. The low-Mo regime favoured FCC plastic accommodation; the intermediate regime favoured combined strengthening and hydrogen management; the high-Mo regime favoured surface durability but required stronger crack-path control.

3.7. Integrated composition–structure–hydrogen–fatigue response

The combined response is summarised in Table 8. Different physical functions were distributed intentionally through the coating thickness rather than being maximised simultaneously at one uniform composition.

Table 9:**Integrated interpretation of the CoCrFeNiMo$_x$ gradient for hydrogen-assisted cryogenic service.**

Coating region	Representative composition	Calculated characteristics	Expected phase character	Hydrogen/fatigue interpretation	Primary function
Substrate-side	x = 0–0.4	δ = 0.302–2.673%; VEC 8.250–8.046	FCC-dominated	Greater plastic accommodation; fewer continuous brittle paths	Interface compliance and cryogenic ductility
Intermediate	x ≈ 0.5–0.6	VEC ≈8; δ ≈ 3%	FCC with σ onset	Strengthening with substantial FCC fraction preserved	Hydrogen-management and strengthening transition
Surface	x = 0.8–1.0	δ = 3.433–3.671%; T_m = 2041–2075 K	FCC/σ eutectic; possible μ	High hardness with stronger crack-connectivity constraint	Wear and surface protection

Within the substrate-side region, comparatively low atomic mismatch and VEC values above approximately 8 were obtained. Predominantly FCC phase stability had also been established experimentally at comparable Mo concentrations. Greater local deformation capacity was therefore supported adjacent to 316L, where an abrupt transition into a σ-rich hard layer could otherwise have intensified strain localisation.

Within the intermediate region, the most balanced combination of calculated and literature-supported mechanisms was obtained. The VEC crossover occurred within approximately 9–13 at.% Mo, lattice distortion had become substantial, and the onset of significant σ formation had been reported in a similar composition interval. Additional

strengthening could therefore have been introduced while a substantial FCC fraction remained available for cyclic deformation accommodation.

Within the surface region, the largest calculated lattice mismatch, density, and melting-temperature descriptors were obtained, while the lowest VEC values were reached. High hardness approaching the 600–700 HV range had been reported for related laser-processed Mo-rich CoCrFeNiMo structures [10,11,14]. Placement of this composition range near the exposed surface was therefore supported for wear resistance. The maximum permissible thickness and phase connectivity of this region, however, could not have been defined from hardness alone because hydrogen-assisted fatigue failure would also have depended on local crack initiation and interphase connectivity.

The coupled response was represented conceptually by

composition gradient → atomic distortion and chemical partitioning → FCC/σ/μ evolution → strength and deformation-mode

Equation (46) was treated as a mechanistic sequence rather than a constitutive relationship. The sequence explained why the highest-Mo composition was not automatically identified as the optimum composition throughout the coating. Increasing Mo promoted favourable mixing energetics, lattice distortion, hardness, and wear resistance, but progressively stronger multiphase development also introduced mechanically vulnerable interfaces. A graded architecture allowed these competing effects to be distributed spatially.

The collective calculations therefore supported an FCC-rich inner zone extending approximately to 9 at.% Mo, a transition zone near 11–13 at.% Mo, and a wear-resistant outer zone near 16.7–20 at.% Mo. The resulting architecture preserved the mechanistic objective of combining substrate compatibility, hydrogen-management capability, cryogenic deformation tolerance, and surface durability without assigning unmeasured fatigue lives, hydrogen concentrations, phase fractions, XRD intensities, EBSD parameters, TDS peak areas, or acoustic-emission classification accuracies to the new coating. Quantities requiring direct experimental measurement remained distinguishable from composition-derived calculations and comparison data, thereby preserving the physical interpretation of the graded material without converting predicted behaviour into artificial experimental evidence.

Conclusion

A coupled composition–thermodynamics–processing–hydrogen–fatigue framework was established for a graded CoCrFeNiMo coating on 316L stainless steel, and the compositional domain was resolved from the CoCrFeNi base state to equiatomic CoCrFeNiMo. Mo content was changed from 0 to 20.00 at.% and from 0 to 29.85 wt.%, while the calculated mixing enthalpy shifted from −3.750 to −4.640 kJ mol $^{-1}$ and the idealised Gibbs free energy of mixing at 298 K shifted from −7.185 to −8.627 kJ mol $^{-1}$. Theoretical density was changed from 8.189 to 8.718 g cm $^{-3}$, and the composition-weighted melting temperature was shifted from 1871.8 to 2075.4 K. Three functional regions were resolved: an FCC-rich inner range containing 0–9.09 at.% Mo, an intermediate range of approximately 11–13 at.% Mo associated with σ-phase onset, and an outer range containing 16.67–20.00 at.% Mo associated with eutectic or hypereutectic FCC/σ structures. Literature-constrained benchmarks showed that graded CoCrFeNi/CoCrFeNiMo architectures had reached 678.6 HV surface hardness with approximately 83% lower wear volume than H13, supporting spatial separation of compliant interfacial and wear-resistant surface functions. The architecture was interpreted as a distribution of interfacial compliance, phase strengthening, hydrogen management, and surface durability rather than uniform maximisation of a single property. A mechanistic basis is therefore provided for connecting local chemistry with phase stability, plastic accommodation, hydrogen trapping, and cyclic damage. Experimental validation will be required through gradient verification, phase-fraction mapping, hydrogen permeation and desorption measurements, cryogenic fatigue testing, residual-stress measurement, and acoustic-emission correlation with crack mechanisms; subsequent work will be directed toward calibrating Ni/Mo feed schedules and hydrogen-sensitive fatigue parameters.

References

[1] Zhou J, Cheng H, Yao N, Lu T, Lu X, Lu F, Li W, Sun B, Zhang X-C, Tu S-T. Temperature dependence of hydrogen embrittlement behavior in a medium-entropy alloy. Acta Mater 2025;298:121396. https://doi.org/10.1016/j.actamat.2025.121396.

[2] Wang Q, Amar A, Jiang C, Luan H, Zhao S, Zhang H, Le G, Liu X, Wang X, Yang X, Li J. CoCrFeNiMo0.2 high entropy alloy by laser melting deposition: Prospective material for low temperature and corrosion resistant applications. Intermetallics (Barking) 2020;119:106727. https://doi.org/10.1016/j.intermet.2020.106727.

[3] Klimova M, Krasanov I, Astakhov I, Kovalenko E, Kochura E, Semenyuk A, Zherebtsov S, Klimova-Korsmik O, Stepanov N. Temperature-dependent mechanical properties of CoCrFeNi medium-entropy alloy produced by laser-directed energy deposition. Metals (Basel) 2025;15:9. https://doi.org/10.3390/met15010009.

[4] Lee DH, An YH, Zhao Y, Lee JH, Kim HY, Kim YS, Lee SY. A novel methodology to estimate hydrogen diffusivity and its applications in revealing hydrogen effects in CoCrNi medium-entropy alloy versus 316L stainless steel. Int J Plast 2023;169:103737. https://doi.org/10.1016/j.ijplas.2023.103737.

[5] Zhu L, Ding C, Li S, Chou TH, Yang T, Liu W, Curtin WA, Wu Z. On the intrinsic resistance to hydrogen embrittlement of equiatomic VCoNi medium entropy alloy. Acta Mater 2026;313:122268. https://doi.org/10.1016/j.actamat.2026.122268.

[6] Zhang Z, Yan S, Yang J, Yin C, Dai P, Qin Q. Additively manufactured CrCoNi/TiC composite exhibiting high strength and superior resistance to hydrogen embrittlement. Mater Charact 2026;233:116133. https://doi.org/10.1016/j.matchar.2026.116133.

[7] Chen T, Su H, Koyama M, Luo H, Wang S, Chen Z, Fu A, Li Y, Zhang Y. Hydrogen embrittlement in a CoCrNi medium-entropy alloy fabricated via laser powder bed fusion: Characteristic intergranular cracking and hydrogen-enhanced twinning. J Mater Sci Technol 2026;240:201–13. https://doi.org/10.1016/j.jmst.2025.03.048.

[8] Liu S, Xu Z, Zhu Y, Shi R, Gao K, Pang X. Superior hydrogen embrittlement resistance of CoCrNi-based medium-entropy alloy via coherent precipitation and grain boundary strengthening. Corros Sci 2024;240:112483. https://doi.org/10.1016/j.corsci.2024.112483.

[9] Ding CD, Jiao ZB, Luan JH, Xu BB, Li R, Cao BX, Zhou CS, Liu WH. Suppressing hydrogen embrittlement of a CrCoNi medium-entropy alloy by triggering co-segregation of carbon, boron, and Cr. Corros Sci 2024;236:112232. https://doi.org/10.1016/j.corsci.2024.112232.

[10] Yu K, Deng L, Zhang M, Tang X, Jin J, Li R, Liu J, Wang X. Laser-clad biomimetic HEA coatings: Synergizing Mo-driven eutectic skeletons and gradient architecture for high wear resistance and interfacial reliability. Surf Coat Technol 2026;531:133561. https://doi.org/10.1016/j.surfcoat.2026.133561.

[11] Sui Q, Wang Z, Wang J, Xu S, Liu B, Yuan Q, Zhao F, Gong L, Liu J. Additive manufacturing of CoCrFeNiMo eutectic high entropy alloy: Microstructure and mechanical properties. J Alloys Compd 2022;913:165239. https://doi.org/10.1016/j.jallcom.2022.165239.

[12] Zhang Q, Li M, Wang Q, Qi F, Kong M, Han B. Investigation of the microstructure and properties of CoCrFeNiMo high-entropy alloy coating prepared through high-speed laser cladding. Coatings 2023;13:1211. https://doi.org/10.3390/coatings13071211.

[13] Li K, Liang J, Zhou J. Microstructure and elevated temperature tribological performance of the CoCrFeNiMo high entropy alloy coatings. Surf Coat Technol 2022;449:128978. https://doi.org/10.1016/j.surfcoat.2022.128978.

[14] Li K, Li X, Zhang P, Zhou J. Effect of molybdenum on the microstructure and elevated temperature tribological properties of CoCrFeNiMox high-entropy coatings prepared by extreme high-speed laser cladding. Surf Coat Technol 2026;519:132965. https://doi.org/10.1016/j.surfcoat.2025.132965.

[15] Wu T, Yu L, Shuai X, Fang Y, Zheng X, Zhang L, Xue Y, Lu Y, Luan B. Microstructure evolution and solidification mechanism of CoCrFeNiMoNb high entropy alloy coating by laser cladding. Intermetallics (Barking) 2024;171:108345. https://doi.org/10.1016/j.intermet.2024.108345.

[16] Cui Y, Shen J, Geng K, Hu S. Fabrication of FeCoCrNiMnAl0.5–FeCoCrNiMnAl gradient HEA coating by laser cladding technique. Surf Coat Technol 2021;412:127077. https://doi.org/10.1016/j.surfcoat.2021.127077.

[17] Zhang Q, Wang Q, Han B, Li M, Hu C, Wang J. Comparative studies on microstructure and properties of CoCrFeMnNi high entropy alloy coatings fabricated by high-speed laser cladding and normal laser cladding. J Alloys Compd 2023;947:169517. https://doi.org/10.1016/j.jallcom.2023.169517.

[18] Wu H, Zhang S, Wang ZY, Zhang CH, Zhang DX, Chen HT, Wu CL. Phase evolution, microstructure, microhardness and corrosion performance of CoCrFeNiNbx high entropy alloy coatings on 316 stainless steel fabricated by laser cladding. Corrosion Engineering, Science and Technology 2022;57:301–10. https://doi.org/10.1080/1478422X.2022.2057273.

[19] Liu N, Zhou Q, Xu M, Niu M, Zhou P, Guo P. Evolution in microstructure, properties of the laser cladding CoCrFeMoNi coatings at different annealing temperatures. Materials Science and Technology 2023;39:2782–91. https://doi.org/10.1080/02670836.2023.2225904.

[20] Jung JY, Jung HW, An YH, Lee SY, Zhao Y, Lau KB, Wang P, Lee DH. Deciphering the role of solidification cell structure in the hydrogen embrittlement of CoCrFeNi medium-entropy alloy fabricated by laser-powder bed fusion: Insights from annealing treatments. Corros Sci 2025;243:112595. https://doi.org/10.1016/j.corsci.2024.112595.

[21] Jeong H, Jeong JY, Lee SY, Ryou KH, Choi PP, Zhao Y, Wei S, Wang P, Lee DH. Effect of boron segregation on hydrogen-induced grain boundary embrittlement in CoCrFeNi medium-entropy alloys. Corros Sci 2025;257:113320. https://doi.org/10.1016/j.corsci.2025.113320.

[22] Wang Z, Jing S, Yan Y. Investigating the mechanisms of hydrogen embrittlement resistance in pre-strained CoCrNi medium-entropy alloy via hydrogen migration and trapping behavior. Materials 2026;19:3010. https://doi.org/10.3390/ma19143010.

[23] Zhao C, Deng L, Wu S, Wu W, Peng Y, Wang X, Jiang Y, Gong J. Dual role of hydrogen in fatigue life of 316L austenitic stainless steel. Int J Fatigue 2025;198:108975. https://doi.org/10.1016/j.ijfatigue.2025.108975.

[24] He S, Ma Y, Zhao D, Song D, He X, Luo S, Wang J. Fatigue crack extension and acoustic emission response law of 316L austenitic stainless steel by hydrogen charging. Theoretical and Applied Fracture Mechanics 2025;138:104983. https://doi.org/10.1016/j.tafmec.2025.104983.

[25] Fu Z, Jiang L, Sun Y, Jin J, Yu C, Zhao M, Kan Q, Kang G. Cyclic deformation and microstructural evolution of 316L stainless steel with pre-charged hydrogen. Int J Fatigue 2024;184:108311. https://doi.org/10.1016/j.ijfatigue.2024.108311.

[26] Povolyaeva E, Klimova M, Yurchenko N, Shaysultanov D, Volkova L, Moskovskikh D, Zherebtsov S, Stepanov N. Fatigue behavior of the carbon-doped CoCrFeMnNi high entropy alloy at cryogenic temperatures. Mater Charact 2025;228:115431. https://doi.org/10.1016/j.matchar.2025.115431.

[27] Rackwitz J, Yu Q, Yang Y, Laplanche G, George EP, Minor AM, Ritchie RO. Effects of cryogenic temperature and grain size on fatigue-crack propagation in the medium-entropy CrCoNi alloy. Acta Mater 2020;200:351–65. https://doi.org/10.1016/j.actamat.2020.09.021.